The Canadian Mineralogist
Vol. 56, pp. 425-449 (2018)
DOI: 10.3749/canmin.1700090

MINERALOGY AND GEOCHEMISTRY OF THE ERONGO SUB-VOLCANIC GRANITE-MIAROLITIC-PEGMATITE COMPLEX, ERONGO, NAMIBIA

ALEXANDER U. FALSTER[§], WILLIAM B. SIMMONS, AND KAREN L. WEBBER

MP[2] Research Group, Maine Mineral & Gem Museum, 99 Main Street, Bethel, Maine 04217

ANDREW P. BOUDREAUX

Gulf of Mexico Business Unit, Chevron Corporation, Covington, Louisiana 70435, U.S.A.

ABSTRACT

The early Cretaceous anorogenic, sub-volcanic Erongo Granite, Namibia, was emplaced into metasedimentary rocks of the Neoproterozoic to Cambrian Damaran Orogeny. The Erongo Granite contains pegmatitic miaroles containing abundant beryllium and boron mineralization and segregations of rounded quartz-tourmaline orbicules (tourmaline nests). This study focuses on the mineralogy of the miarolitic pegmatites and quartz-tourmaline orbicules and the geochemistry of the Erongo Granite. Erongo miarolitic pegmatites are famous for spectacular mineral specimens of schorl, foitite, aquamarine, topaz, fluorite, and jeremejevite. Mineral samples from three areas where artisanal mining exposed miarolitic cavities were examined: Lion's Head (LH), Hohenstein Gorge (HG), and Tubusis (TB). Tourmaline, biotite, and associated minerals were investigated from granite, miarolitic cavities, and quartz-tourmaline orbicules from these three areas. Whole-rock geochemical analyses of granites from the LH and HG locations were also performed. The LH and HG granites have different modal mineralogy, with LH richer in plagioclase and HG richer in biotite and quartz and slightly richer in K-feldspar; both are unusually rich in B for anorogenic granite.

Biotite occurs principally in the granite and is typically absent in miarolitic cavities and quartz-tourmaline orbicules, where the iron-rich phase is tourmaline. The micas range from Mg-siderophyllite to annite in LH granite, are Li-rich siderophyllite in HG granite, and are annite in TB granite, using the classification of Tischendorf *et al*. (1997). Micas in both the LH and HG tourmaline nests are Li-rich siderophyllite. All mica is Fe dominant at the Y-site, with variable contents of the lesser Y-site occupants. The LH mica has significantly more trivalent iron, suggesting that conditions may have been more oxidizing than in the HG location.

Tourmaline from granite ranges from iron-rich schorl with low to intermediate X-site vacancies to lower-iron schorl. Tourmaline from miarolitic cavities is dominantly schorl and fluor-schorl. The H_2O content of schorl determined by LOI is very similar to H_2O calculated by stoichiometry for the EMP analyses (3.23_{av} calc *versus* 3.35_{av} LOI), thus we infer that the oxygen content of the V-site in schorl is low. Prismatic schorl crystals from some miarolitic pockets are etched and altered to foitite at their ends. Rare color-zoned tourmaline was found in millimeter-size crystals in one pocket. Beryl, topaz, fluorite, and jeremejevite show little chemical variation throughout the complex.

Whole rock geochemical analyses of the granites show both LH and HG to be peraluminous, sub-alkaline, and relatively low in HFSE. Chondrite-normalized REE plots show both granites to be only slightly enriched in LREE. Plots are relatively flat with a strong negative Eu anomaly. Relative to continental crust, Erongo Granite samples are depleted in Ba, Sr, and Ti and relatively enriched in Zr, Nb, Th, U, Y, and REE. There are, however, distinct chemical differences between the two locations. The LH granite is more calc-alkaline and more enriched in LREE; the HG granite is more tholeitic and enriched in Rb, Cs, HREE, and Y with a much flatter CN REE plot with a stronger negative Eu anomaly. Tectonic discrimination diagrams (Pearce *et al*. 1984) show that the LH and HG granites do not plot strictly in the WPG field but have a mixed geochemical signature; the LH granites plot in the VAG-syn-COLG field whereas HG granites plot along the syn-COLG and WPG boundary. We interpret that this mixed geochemical signature results from substantial contamination from the metasedimentary rocks of the Damara orogen altering the geochemistry from a more typical A-type granite toward the VAG-syn-COLG field and introducing B to the melt that eventually became the Erongo Granite and produced the boron-rich miarolitic pegmatites.

The geochemical signature of the Damara orogen is most evident in the quartz-tourmaline orbicules and miarolitic cavities, where volatile and incompatible elements were sufficiently concentrated *via* fractional crystallization to cause exsolution of a second fluid phase, crystallization of tourmaline, and the development of pegmatitic textural and mineralogical changes.

Keywords: pegmatite, Erongo, miarolitic, schorl, contaminated anorogenic pegmatite.

§ *Corresponding author e-mail address*: afalster@mainemineralmuseum.org

Introduction

Erongo pegmatites are famous for spectacular mineral specimens of schorl, foitite, aquamarine, topaz, fluorite, and jeremejevite. The pegmatites occur in the sub-volcanic Erongo Granite in the Erongo caldera complex about 40 km north of Usakos, Namibia. The rift-related anorogenic igneous activity is related to the breakup of Gondwana in the early Cretaceous (~145 Ma) (Bowden *et al*. 1990) with an age of ~133 to 132 Ma for the Erongo Granite (Wigand *et al*. 2004). The Erongo mountains are the erosional remnant of a bowl-shaped volcanic massif, intruded by resurgent granodiorite and granite bodies. It is one of several anorogenic volcanic-plutonic complexes in western Namibia. The Erongo pegmatites occur as segregations of miarolitic cavities in the sub-volcanic granite and are unusual in that they have very elevated levels of boron, more than is typical of anorogenic pegmatites. The high boron concentration is expressed as abundant tourmaline mineralization within the pegmatitic cavities, numerous small quartz-tourmaline orbicules in the granite, and as a rare accessory mineral in the host granite. Two species of tourmaline have been documented from the Erongo Granite, including schorl and foitite. In addition, the Erongo Granite is one of only a few locations worldwide known to host jeremejevite, a rare aluminoborate mineral. This study focuses on the mineralogy of the miarolitic pegmatites, the quartz-tourmaline orbicules, and the whole-rock geochemistry of the granite to better understand the origin of the pegmatites and the abundant boron mineralization. Mineral samples from three areas within the Erongo Granite where artisanal mining exposed miarolitic cavities were examined: the Lions Head (LH), Hohenstein Gorge (HG), and Tubusis (TB) areas (Figs. 1–4). Tourmaline and biotite minerals were investigated from granite, miarolitic cavities, and quartz-tourmaline orbicules (tourmaline nests, TN). Beryl, topaz, fluorite, and jeremejevite from within miarolitic pegmatites were also investigated. Whole-rock geochemical analyses of granites from the LH and HG locations were also performed.

Crystals in the miarolitic cavities can attain several centimeters in length and girth. Two species of tourmaline, schorl and foitite, have been previously documented from the Erongo Granite (Cairncross & Bahmann 2006). Trumbull *et al*. (2008) performed geochemical and isotopic studies of tourmaline from the Erongo Granite and its potential source rocks, but prior to this study no detailed analyses were done to relate the mineral chemistry of the pegmatites and orbicules to the composition of the hosting parent granite.

Geologic Setting

The Erongo Granite is one of several rock units comprising the Erongo Igneous Complex, located in west-central Namibia, Africa (~15.5°S, 21.5°E). The complex is described by Trumbull *et al*. (2008) as the erosional remnant of a bowl-shaped volcanic massif, cross-cut by resurgent plugs of granodiorite and granite bodies. It is one of several anorogenic, subvolcanic complexes emplaced into the Damara orogenic belt, which formed during the Neoproterozoic to Cambrian collision of the Congo and Kalahari cratons (Fig. 3).

These early Cretaceous anorogenic complexes are thought to be genetically associated with the Tristan da Cunha mantle plume, the Paraná-Etendeka Large Igneous Province, and the eventual rifting of western Gondwana into the African and South American continents (Haapala *et al*. 2007).

The Erongo complex was first described by Cloos (1911, 1919) and then much later and in more detail by Emmermann (1979) and Blümel *et al*. (1979). Pirajno (1990) investigated the Erongo complex using topographic maps, aerial and satellite photography, and petrological studies of all igneous units to provide a comprehensive geological interpretation. Wigand *et al*. (2004) placed detailed temporal constraints on magmatic activity within the complex using Ar-Ar and U-Pb dating, concluding that the duration of emplacement of most units was relatively short-lived (136–130 Ma).

Trumbull *et al*. performed a number of studies, including isotopic relationships between the anorogenic intrusives and potential source rocks (2000, 2004), the isotopic signature of boron from tourmaline within the Erongo Granite and basement schists (2008), and the role of REE-Y-Th-U-bearing accessory minerals in the Erongo Granite (2010). Cairncross & Bahmann (2006) and von Bezing *et al*. (2007) give a detailed account of mineral specimens found within pegmatitic cavities at Erongo.

The geologic map (Fig. 4) shows the igneous members comprising the Erongo complex. Volcanic stratigraphy and the cross-cutting relationships of the plutons (Wigand *et al*. 2004) show a compositional trend from mafic to felsic magmas over the duration of igneous activity. This supports a model in which the basalt and intermediate-composition pyroclastic flows were later intruded by intermediate, felsic, and eventually undersaturated alkaline plutons (Pirajno 1990). This apparent shift in magma composition is thought to be the result of melt source-location changing from the upper mantle to the crust (Schneider 2004). Emmermann (1979) noted the peraluminous chemistry, presence of cordierite, and

FIG. 1. Google Earth imagery showing spheroidal outcrops in the Lions Head location. LH area of artisanal mining and sample sites is encircled.

abundant crustal xenoliths in both the older Ombu Granodiorite and Rhyodacite and proposed derivation from local basement rocks.

The Erongo Granite was emplaced during the later stages of activity in the Erongo complex and is volumetrically the most important intrusive phase (Schneider 2004). The age of the Erongo Granite has been well constrained to ~132–133 Ma *via* $^{40}Ar/^{39}Ar$ stepwise heating of biotite and U-Pb dating of zircon samples (Wigand *et al*. 2004). Pirajno (1990) noted that the intrusion of the Erongo Granite (1) may have vented through ring fractures around the complex, producing compositionally equivalent rhyolites (Ekuta Rhyolite); (2) was perhaps coeval with the collapse of

FIG. 2. Hohenstein Gorge, Hohenstein Mountain. Dashed lines outline the gorge.

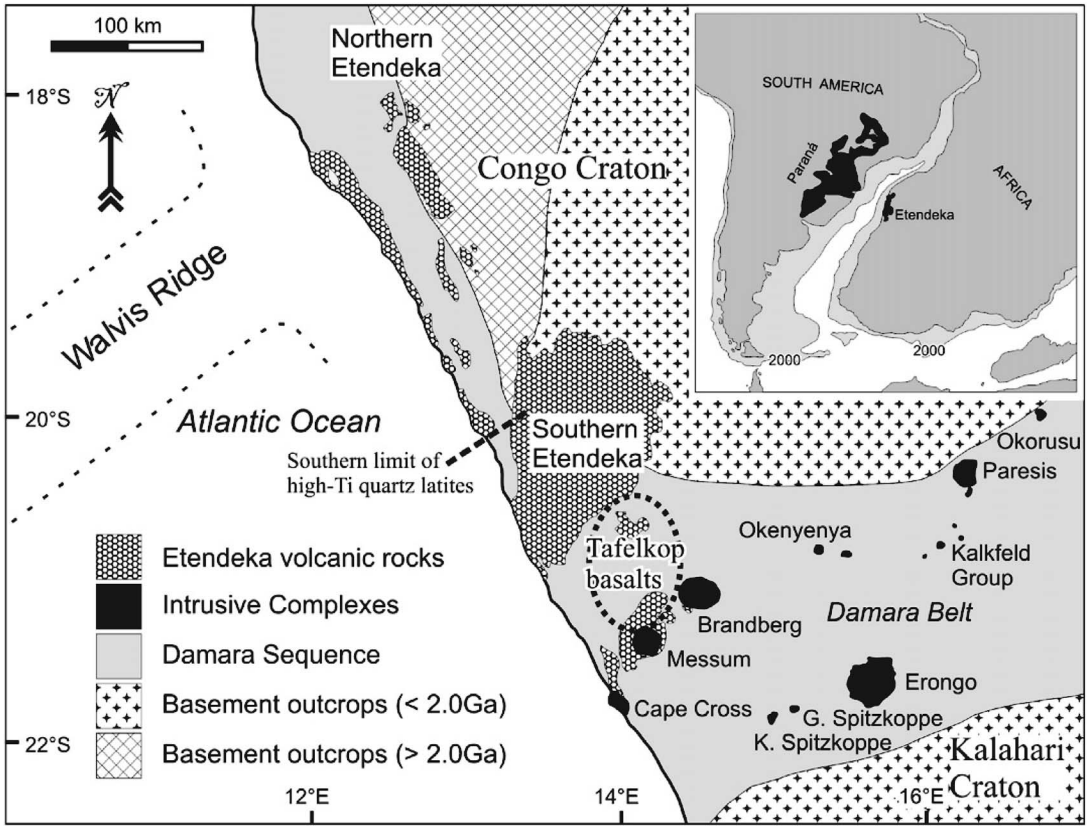

FIG. 3. Geologic features of northwest Namibia from Haapala *et al*. (2007) showing the Erongo and other intrusive complexes within the Damara orogenic zone.

the volcanic structure and the formation of the Erongo caldera; and (3) eventually led to B-rich fluid exsolution and localized, greisen-type W, Sn, F, and Be mineralization.

MINERALS

Biotite

Biotite is a minor rock-forming mineral in all whole-rock samples of the Erongo Granite, ranging from 1.6 to 7.5 modal percent. It occurs in tourmaline nests and miarolitic cavities where tourmaline is the dominant ferroan phase. Representative electron microprobe analyses are given in Table 1. Biotite analyses were recalculated on the basis of 12 anions per formula unit (Table 1) and plotted in the Fe_{tot}+Mn+Ti-Al^{VI} *apfu versus* Mg-Li *apfu* diagram after Tischendorf *et al*. (1997) for the classification of Li-bearing micas (Fig. 5), modified with the latest IMA nomenclature (Rieder *et al*. 1998). The ferric iron content of biotite was determined by titration using the method described in Appendix 1. The LH biotite samples have a higher ferric iron component, with FeO / FeO_{tot} = 0.40. Biotite samples from HG and TB contain a much lower ferric iron component, with FeO / FeO_{tot} = 0.88. The highest FeO is 27.15 wt.% from TB. Micas from the LH granite contain up to 26.71 wt.% FeO. The highest ferric iron component is 19.16 wt.% from the LH mica. Micas from the HG and TB locations contain the lowest ferric iron component, ranging down to 3.31 wt.%.

Analyzed samples have a range of compositions at the Y-site and plot in several fields of the diagram (Fig. 5). Iron is the dominant cation at the Y-site in all samples. LH micas from granite cluster in the field of annite and Mg-rich siderophyllite. Micas from TB also cluster in the annite field but are slightly richer in Li than those from LH. The HG micas also segregate into two groups, the high-iron Li-rich siderophyllite and lower-iron Li-rich siderophyllite, both with similar Li content. Micas from TN plot in the Fe-rich area of the Li-rich siderophyllite field. The data do not reveal any

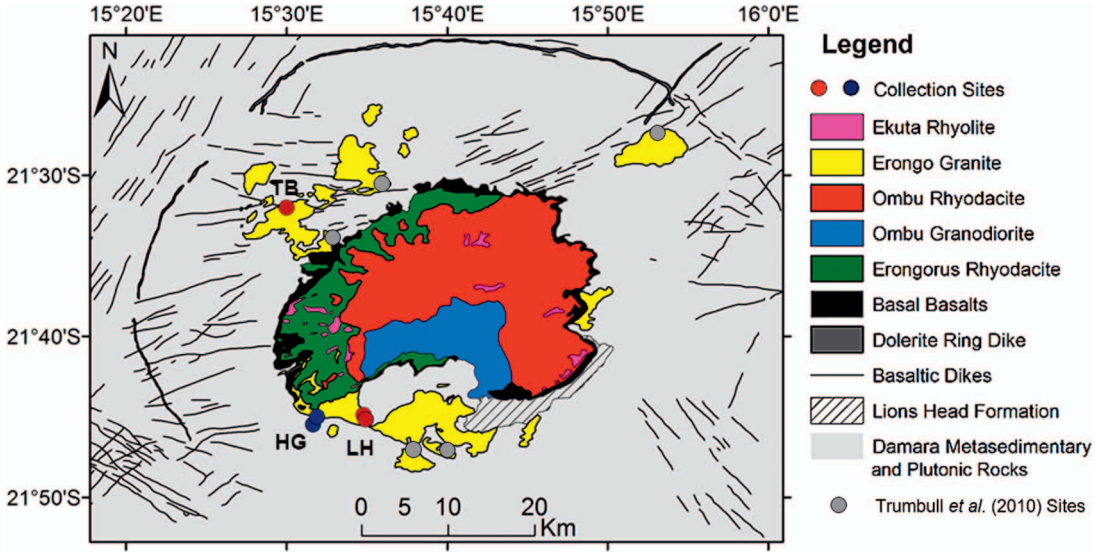

FIG. 4. Simplified geologic map of the Erongo complex showing the regional position of the complex, a list of rock types from Wigand *et al*. (2004) and the Lions Head (LH), Hohenstein Gorge (HG), Tubusis (TB), and Trumbull *et al*. (2010) sample locations.

obvious trends in biotite composition from granite to quartz-tourmaline orbicules. Biotite is largely absent in miarolitic cavities and TN, where schorl is the dominant ferroan phase. Some LH mica has significantly more trivalent iron, suggesting that conditions were more oxidizing in that location.

Feldspars

Albite is the only plagioclase feldspar found in the Erongo Granite. It is the third most-abundant mineral and occurs in white, colorless, and pale tan crystals up to 5 cm in maximum dimension. Table 2 shows albite electron microprobe (EMP) results from HG and LH. The results are similar for both locations: Na_2O ranges from 11.49 to 11.65 wt.% and CaO only attains 0.01 to 0.51 wt.%.

Orthoclase is a major constituent of the Erongo Granite. The K-feldspar has a microperthitic texture and is structurally orthoclase. Crystals may exceed 20 cm in maximum dimension. The color ranges from white to tan and some pale-green amazonite has also been found. Effects of slight to intense etching are commonly evident. Twins after the Carlsbad, Manebach, and Baveno laws are common. Analytical data for orthoclase are shown in Table 2.

Albite samples have an An-content that ranges from 0.0 to 3.6%. The K/Rb *apfu* ratio of K-feldspar samples ranges from 436 to 1607, with an average value near the lower end of the range at 771. Separated based on sample class, the average K/Rb *apfu* values of K-feldspar are 804 in granite samples and 720 in miarolitic-cavity samples. These values show a slight increase in Rb substitution from granite to miarolitic-cavity samples. Orthoclase shows exsolution lamellae but no gridiron twinning as is seen in microcline. Thus, the Na content of the K-feldspar component is low. Orthoclase was confirmed by X-ray diffraction.

Tourmaline species

Most Erongo tourmaline is schorl. It occurs as a rare accessory mineral in the granite and in segregations of TN. It is unclear whether the tourmaline in the granite is primary or related to the quartz-tourmaline segregations. The largest and most spectacular schorl crystals occur in miarolitic cavities (Figs. 6–7). Many crystals are very well-crystallized with lustrous faces. Crystals showing mosaic texture or splitting near the termination into fibrous tourmaline are widespread. The pockets contain lustrous crystals up to 15 cm and some may contain kilos of crystals. In some cavities prismatic schorl appears to have been etched and altered. The antilogous ends of the crystals appear to be most affected (Fig. 7).

A few small, color-zoned tourmalines (Fig. 8) were recovered by performing heavy mineral separations on miarolitic cavity gravel. Color-zoned crystals were generally 2 to 5 mm in length and often contained schorl overgrown by a clear to brownish-colored

TABLE 1. REPRESENTATIVE EMP COMPOSITIONS OF BIOTITE

wt.%	HG-2-bio1	LH-8-bio2	HG-1-bio2	HG-1-bio1	LH-2-bio1	TB-2-bio2
SiO_2	38.32	36.54	36.73	37.70	37.31	36.70
TiO_2	0.99	4.11	2.58	1.27	2.09	2.56
Al_2O_3	19.93	13.42	13.98	15.90	15.49	13.80
Fe_2O_3	3.31	19.16	4.18	4.20	4.17	4.24
FeO	21.23	11.74	26.81	26.91	26.71	27.15
FeO_{tot}	24.20	28.98	30.57	30.69	30.46	30.97
MnO	0.98	0.34	0.11	0.18	0.09	0.13
MgO	0.22	1.28	1.87	0.17	0.11	0.17
CaO	0.01	bdl	bdl	bdl	bdl	bdl
Na_2O	0.03	0.03	0.03	0.03	0.04	0.04
K_2O	8.72	8.45	8.65	9.00	8.78	8.63
Rb_2O	0.01	0.02	0.02	0.02	0.02	0.02
Li_2O(est.)	1.42	0.90	0.96	1.24	1.13	0.95
H_2O(calc.)	3.36	3.48	3.22	3.32	3.30	3.20
F	1.22	0.93	1.22	1.11	1.11	1.12
$F \equiv O$	–0.51	–0.39	–0.51	–0.47	–0.47	–0.47
Total	99.26	100.02	99.86	100.57	99.88	98.24
apfu						
K	0.847	0.824	0.870	0.894	0.878	0.884
Ca	0.001	bdl	bdl	bdl	bdl	bdl
Na	0.005	0.005	0.005	0.004	0.006	0.007
Rb	0.001	0.001	0.001	0.001	0.001	0.001
Σ X	0.853	0.829	0.876	0.899	0.885	0.892
Fe^{2+}	1.352	0.751	1.767	1.752	1.750	1.824
Fe^{3+}	0.190	1.102	0.248	0.246	0.246	0.256
Mg	0.025	0.146	0.220	0.020	0.013	0.020
Mn	0.063	0.022	0.008	0.012	0.006	0.009
Ti	0.057	0.236	0.153	0.074	0.123	0.155
Al	0.706	0.003	0.194	0.393	0.355	0.254
Li(est.)	0.434	0.278	0.304	0.387	0.355	0.306
Σ Y	2.827	2.538	2.893	2.883	2.849	2.824
Si	2.917	2.794	2.895	2.934	2.924	2.948
Al	1.083	1.206	1.105	1.066	1.076	1.052
Σ T	4.000	4.000	4.000	4.000	4.000	4.000
H(calc.)	1.706	1.774	1.695	1.726	1.725	1.716
F	0.294	0.226	0.305	0.274	0.275	0.284
Σ W	2.000	2.000	2.000	2.000	2.000	2.000

Cs and P analyzed for but not detected; *apfu* calculated based on 12 anions per formula unit; H calculated by stoichiometry; Li estimated by the equation: $0.289SiO_2$–9.658 (Tischendorf *et al.* 1997); bdl = below detection limit.

species. Some analyses of the light-colored portions of color-zoned tourmaline (Fig. 8) appear to possibly be rossmanite, but further work is required to confirm if their Li content is high enough for rossmanite.

Striking features visible in the Erongo Granite are segregations of quartz-tourmaline orbicules (Fig. 9). They stand out as dark oval blebs surrounded by a light-colored halo. The orbicules are composed of 56% tourmaline and 44% quartz, with minor amounts of accessory fluorite, apatite, topaz, and cassiterite. The halos consist of K-feldspar and quartz and are depleted in mafic minerals. The quartz-tourmaline orbicules appear to have formed as segregations of immiscible quartz and tourmaline.

Representative Erongo tourmaline analyses are given in Table 3 and are plotted in classification diagrams (Figs. 10–12) and colored to represent hosting lithology. A ternary plot for X-site composition shows a wide compositional range for granites, tourmaline orbicules, and miarolitic cavities. Compositions range from alkali group to slightly X-site vacant, with very low Ca content. The X-site vacant compositions are all from miaroles (Fig. 10) The X-site alkali samples are Fe-rich, Mg-poor, and have low Li content. The measured Li is insufficient to fill the

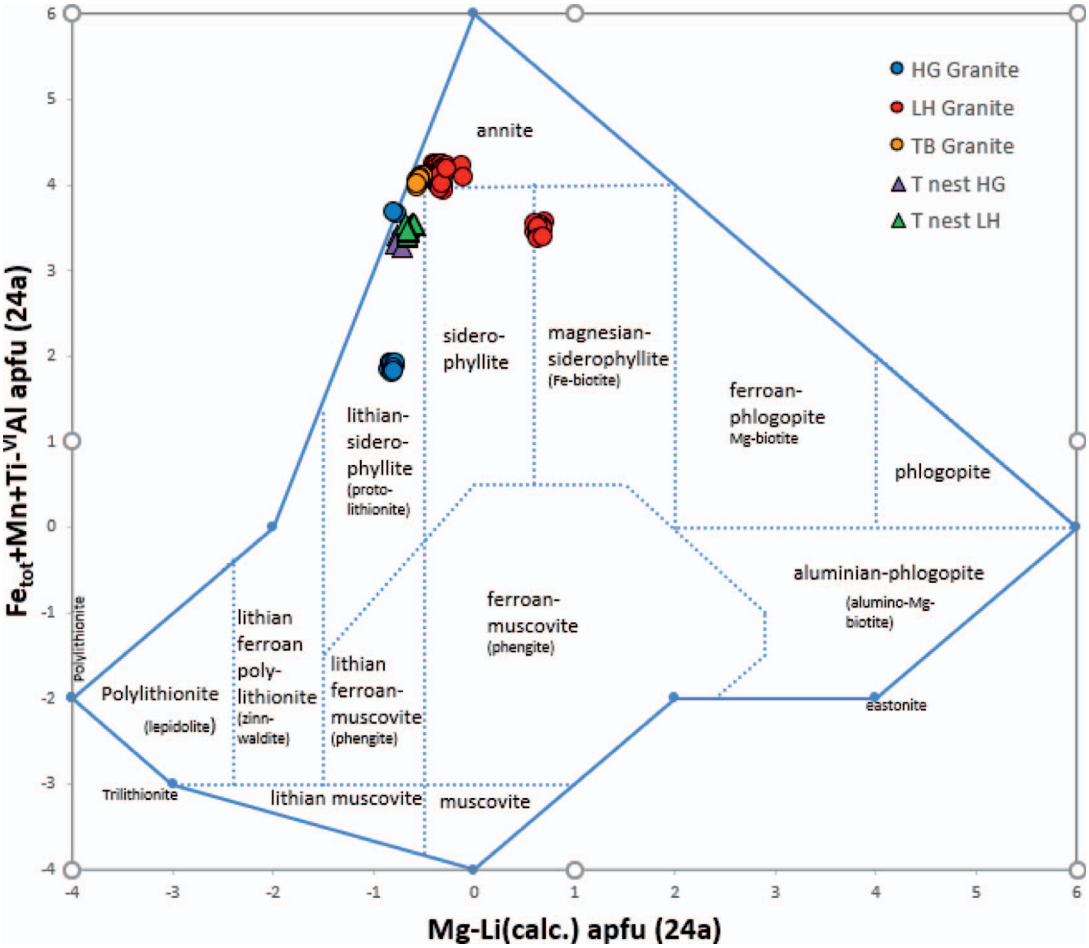

FIG. 5. Mica compositions plotted on the Fe_{tot}+Mn+Ti-Al^{VI} *apfu versus* Mg-Li *apfu* diagram of Tischendorf *et al*. (1997).

Y-site. We report Li calculated by stoichiometry. Water content of 10 selected tourmaline crystals from miarolitic cavities was measured by LOI. H_2O content of schorl averages 3.35 wt.% H_2O. This value matches very well with the average water content of 3.23 wt.% calculated by stoichiometry for the EMP analyses. Thus, we infer that the V-site oxygen content for schorl is very low.

Figure 11 shows the Na/(Na + X-site vac) *apfu* ratio *versus* YAl/(YAl + Fe) *apfu* ratio diagram of Selway *et al*. (2000) for all tourmaline samples. All granite tourmaline samples are schorl. LH tourmaline from granite has the highest Na content. The HG and TB tourmaline from granite are similar, but HG have a tighter range of Fe content with lower Na than tourmaline from LH granite. The LH tourmaline orbicules are lower in Na than tourmaline from the LH granite. The TN from HG are richer in Fe and slightly richer in Na than TN from LH. Tourmaline nests from HG are the richest in Fe content. Tourmaline from LH miaroles show a wide range in Na content, from schorl to foitite. The TB tourmaline in miaroles is similar to that of LH miaroles. The HG miarolitic tourmalines show a large range in Fe and Na content with compositions ranging from schorl to foitite. Trumbull *et al*. (2008) tourmaline data are all very Fe rich with similar Na content as the TB granite tourmalines.

Figure 12 shows the W-site F *apfu* plotted against X-site vacancies *apfu* for all tourmaline samples. Overall, the data straddle the dividing line between OH and F schorl but slightly favor OH-dominance. All foitite species were found to be hydroxyl-dominant. Tourmaline from the granites ranges from schorl to fluor-schorl. The LH granite tourmalines are both schorl and fluor-schorl. The TB tourmaline from

TABLE 2. REPRESENTATIVE EMP COMPOSITIONS OF ALBITE AND ORTHOCLASE

wt.%	HG-fs2	HG-fs3	LH-fs7	LH-fs6	TB-fs3	TB-fs6	HG-fs1	HG-fs5	LH-fs4	LH-fs3	TB-fs1	TB-fs3
SiO_2	68.39	68.54	68.48	68.57	68.51	68.46	64.52	64.49	64.66	64.54	64.61	64.51
TiO_2	bdl	0.01	bdl	0.01	0.01	0.01	0.02	0.02	0.03	0.01	0.01	0.03
Al_2O_3	19.46	19.48	19.48	19.54	19.46	19.54	18.52	18.48	18.40	18.53	18.46	18.54
FeO_t	0.01	0.01	0.01	0.01	0.01	0.01	0.02	0.02	0.02	0.02	0.02	0.02
CaO	0.12	0.51	0.09	0.19	0.29	0.14	0.02	0.09	0.03	0.03	0.03	0.05
Na_2O	11.61	11.49	11.56	11.45	11.30	11.44	0.23	0.17	0.13	0.29	0.22	0.19
K_2O	0.06	0.02	0.02	0.06	0.03	0.02	16.57	16.60	16.66	16.45	16.51	16.54
Rb_2O							0.03	0.04	0.06	0.04	0.05	0.06
Total	99.65	100.06	99.64	99.81	99.60	99.63	99.94	99.92	99.98	99.92	99.92	99.93
apfu												
K	0.003	0.001	0.001	0.003	0.002	0.001	0.979	0.982	0.984	0.972	0.976	0.978
Na	0.986	0.973	0.981	0.970	0.959	0.971	0.021	0.016	0.012	0.026	0.020	0.017
Ca	0.005	0.024	0.004	0.009	0.014	0.007	0.001	0.005	0.002	0.002	0.002	0.002
Rb							0.000	0.001	0.001	0.001	0.002	0.001
Σ X	0.995	0.998	0.987	0.982	0.975	0.979	1.001	1.002	0.999	1.000	0.999	0.998
Al	1.000	1.000	1.000	1.000	1.000	1.000	0.999	0.999	0.999	0.999	0.999	0.999
Fe	0.000	0.000	0.000	0.000	0.000	0.000	0.001	0.001	0.001	0.001	0.001	0.001
Σ Y	1.000	1.000	1.000	1.000	1.000	1.000	1.000	1.000	1.000	1.000	1.000	1.000
Si	2.996	2.992	2.998	2.997	3.000	2.997	2.989	2.989	2.994	2.989	2.993	2.988
Ti	bdl	0.000	bdl	0.000	0.000	0.000	0.001	0.001	0.001	0.000	0.000	0.001
Al	0.005	0.002	0.006	0.007	0.004	0.009	0.012	0.011	0.005	0.012	0.009	0.013
Σ Z	3.001	2.995	3.004	3.004	3.004	3.006	3.002	3.000	3.001	3.002	3.002	3.003
An %	0.5	2.4	0.4	0.9	1.4	0.7						

Mg, Mn, Ba, Sr, Cs, and Rb analyzed for but not detected; *apfu* calculated based on 8 anions per formula unit; bdl = below detection limit.

granite is similar to LH but has slightly higher OH. Tourmaline from HG granite consists only of schorl. Tourmaline from orbicules in the LH are all OH-dominant (see oval fields in Fig. 12). Tourmaline from the quartz-tourmaline nests in HG are all fluor-schorl. Tourmalines from the miarolitic cavities are both F- and OH-rich and show no trend between locations.

Foitite compositions are found at the ends of crystals that appear to have been corroded and altered. Sections of prismatic crystals were analyzed along their length to study the zoning. The crystals are zoned from schorl to foitite along their length. The fibrous ends of the crystals are foitite in composition (Fig. 13).

The quartz-tourmaline orbicules appear to have formed as segregations of immiscible quartz and tourmaline, possibly fluxed by high fluorine. The Mg content of all schorl is low, ranging from 0.0 to 2.37 wt.% MgO. A few examples from miarolitic pockets in LH and HG show slight enrichment in Mg. A few HG miaroles have tourmaline with the higher MgO content, up to 2.37 wt.%. The source of this Mg enrichment is uncertain but could be from the alteration of biotite adjacent to the pockets. Most miarolitic tourmaline is, however, low in Mg.

In summary, the following points are noted for the Erongo tourmaline:

- Though much more abundant in miarolitic cavities and quartz-tourmaline orbicules, the presence of tourmaline in all granite samples attests to significant B- and H_2O-enrichment of the Erongo pluton.
- Fluor-schorl is confirmed for the first time.
- No apparent trend in W-site F or OH dominance with respect to type of occurrence (granite, TN, or miaroles) is apparent.
- Tourmaline compositions trend from Na- and Fe-dominant schorl to X-site-vacancy dominant foitite.
- More evolved color-zoned tourmaline, probably rossmanite, only occurs in miarolitic cavities.

Beryl

The Erongo Mountains are renowned for gem-quality aquamarine crystals. Crystals of beryl are generally well-formed and light blue to light green in color, but color-zoned, white, and colorless crystals are also common (Fig. 14). Beryl is widespread and found in nearly all miarolitic cavity samples but was not

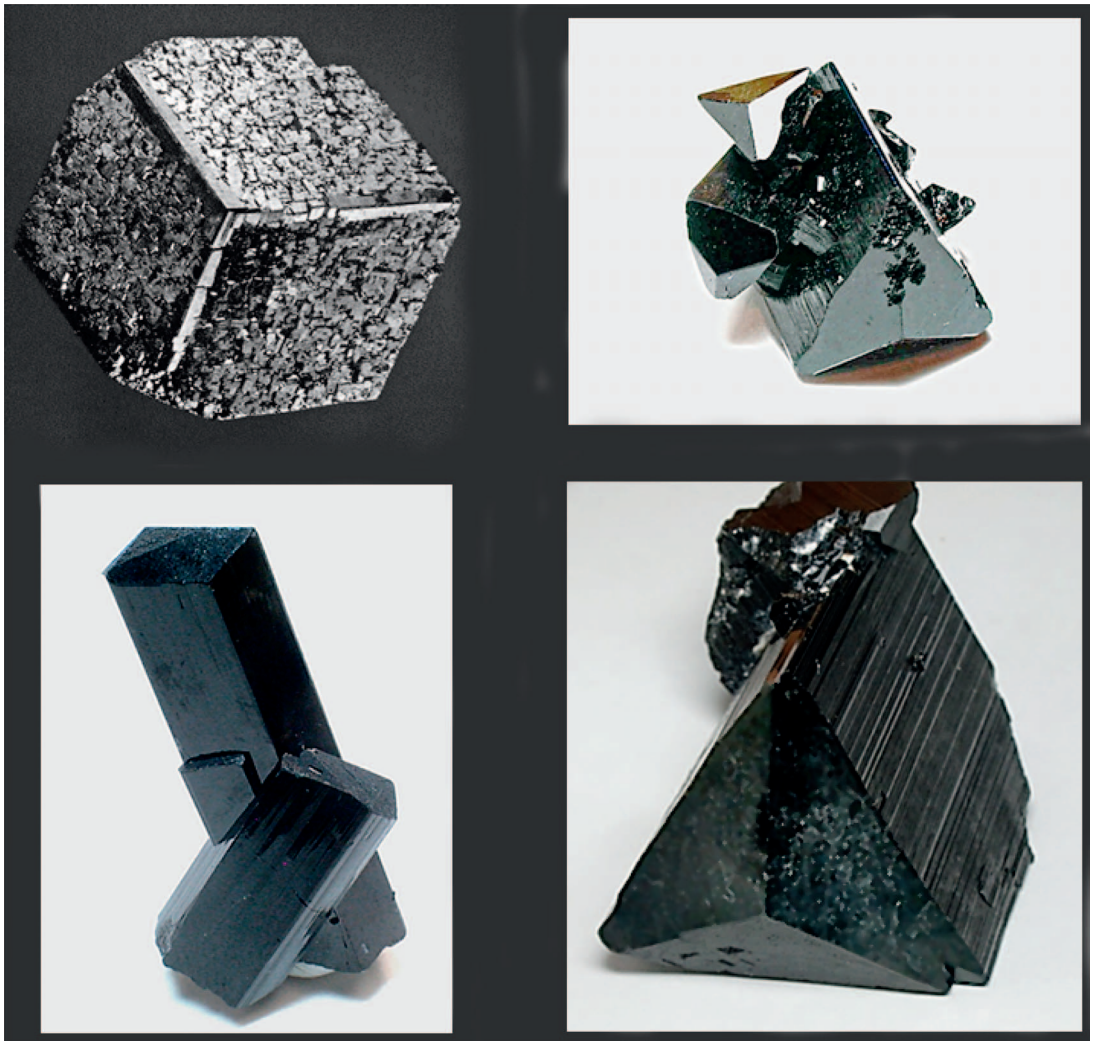

FIG. 6. Examples of schorl crystals from the Erongo Mountains. Field of view for all images is 4 cm.

found in granite or quartz-tourmaline nest samples. Prisms and pinacoids are dominant forms; dipyramids are generally small and may be missing altogether. Crystals may attain over 10 cm in length, but 1–5 cm is a more common size. Beryl EMP analyses are shown in Table 4. Beryls from HG and LH are chemically very similar and show no significant variation from the different miaroles. Na_2O ranges from 0.13 to 0.31 wt.%. Beryl only contains minor amounts of FeO (0.10–0.34 wt.%) and Sc_2O_3 (0–0.02 wt.%).

Jeremejevite

Jeremejevite is an extremely rare aluminoborate mineral, $Al_6B_5O_{15}(F,OH)_3$, known from only four other locations worldwide. It has been documented in Myanmar, Germany, Tajikistan, Eastern Siberia, and the Erongo Region of Namibia. Jeremejevite from the Erongo Granite area is colorless to intense blue in color and highly coveted for gemstock and collection pieces. Crystals from the Erongo Mountains attain 5 cm in length and only occur in miaroles. Jeremejevite is chemically near-ideal stoichiometry. Trace amounts of TiO_2 up to 0.02 wt.%, FeO up to 0.04 wt.%, and CaO up to 0.10 wt.% are present.

Ilmenite-pyrophanite

Ilmenite-pyrophanite was abundant in the heavy mineral separates of granite samples from the LH area

FIG. 7. Top: Schorl crystal showing splitting into numerous long-prismatic foitite crystals near the termination (6 cm). Bottom: Fibrous composite foitite crystals (4 cm).

and as inclusions within biotite in samples from HG and TB. Ilmenite–pyrophanite analyses are given in Table 5. Observed maximum crystal size is over 7 cm. Ilmenite–pyrophanite composition ranges from ilmenite-dominant to pyrophanite-dominant.

Topaz

Topaz is abundant in granite and in miarolitic cavity samples, and to a lesser extent in TN samples. The largest topaz crystal found had a maximum dimension of 20 cm. Colorless crystals are most common, but pale blue or pale green topaz has been found. Overall, the analyzed topaz crystals have a high purity, showing very little substitution of other elements for stoichiometric aluminum and silicon. The hydroxyl component in the topaz samples of the Erongo Granite is consistently low, with nearly all samples having less than 0.20 *apfu* OH substitution at the F structural site. There is, however, a noticeable distinction between relatively OH-rich topaz from miarolitic cavities and quartz-tourmaline nests and OH-depleted topaz from granite samples.

Fluorite

Fluorite is a common accessory mineral in granite and TN samples. Large fluorites, typically

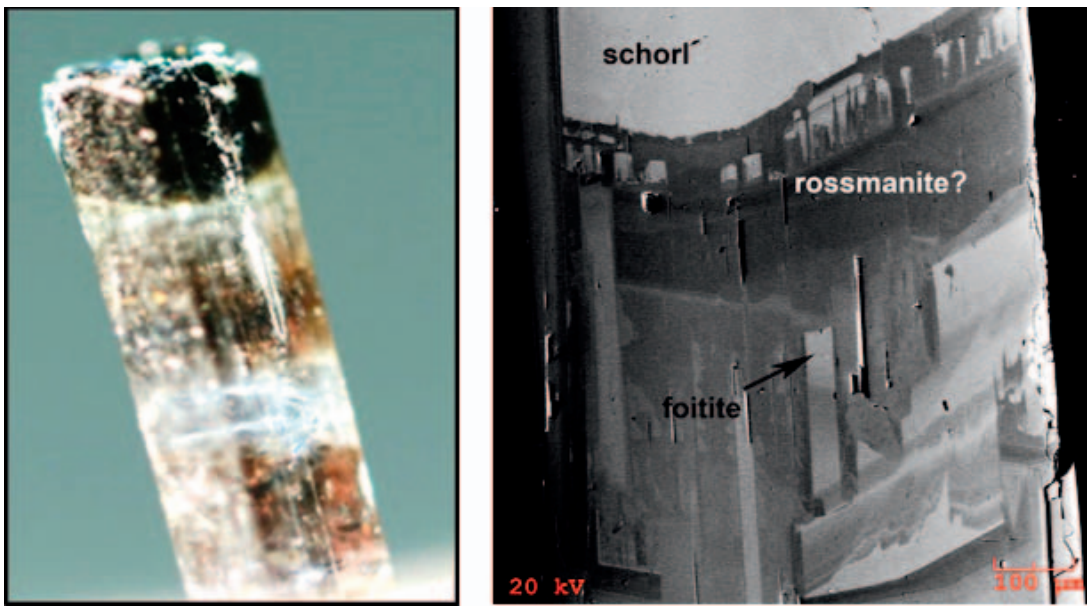

FIG. 8. Color-zoned tourmaline crystal from a miarolitic cavity in HG (3 mm) and backscattered electron image showing three possible species: schorl, foitite, and possibly rossmanite (darkest bands); further work is needed to confirm if these areas contain sufficient Li to be rossmanite.

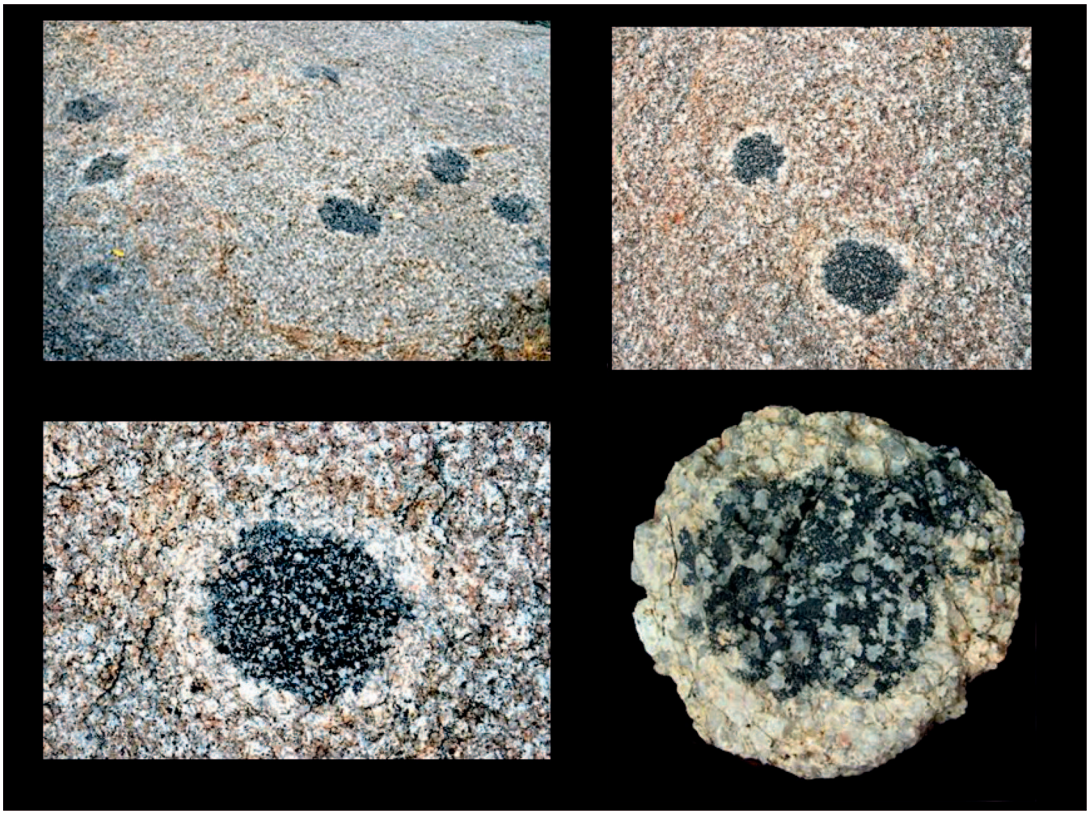

FIG. 9. Examples of quartz-tourmaline orbicules (TN) from the Erongo Mountains, ~20 cm across. Note pronounced depletion halos.

in cubic or mixed cubic/octahedral forms, are commonly found as euhedral crystals in miarolitic cavities. Fluorite found within the granitic matrix is nearly always colorless to slightly purple, whereas miarolitic cavity fluorites are dominantly green. Color-zoned green/purple cube and cube-octahedra crystals are common. Maximum crystal size is about 10 cm. Analytical results for fluorite are given in Table 6. Fluorite contains REE in concentrations up to approximately 100 ppm. The overall pattern is very similar to the whole-rock chondrite-normalized pattern (Fig. 15). The plot is relatively flat with a pronounced negative Eu anomaly. The REE enrichment in Erongo fluorite is lower and flatter than that of fluorite from other anorogenic pegmatites such as Moat Mountain USA (Camp 2011). Fluorite has anomalous positive spikes for Sm and Yb. Ytterbium spikes are seen in fluorite from other anorogenic miarolitic pegmatites, but the Sm spike is unusual and not explained.

WHOLE-ROCK GEOCHEMISTRY

Whole-rock geochemical data were obtained from HG and LH. Fusion ICP-OES and ICP-MS were the primary analytical methods for major and trace elements. Fluorine was quantified by EMP analysis of flash-fused samples using the method of Simmons *et al*. (2016), and boron and lithium concentrations were determined *via* DCP spectrophotometry. Whole-rock analytical results for LH and HG granites are given in Table 7.

For comparative purposes, geochemical data from Trumbull *et al*. (2010) and Pirajno (1990) were included in this study. Whole-rock sampling locations from this study and from Trumbull *et al*. (2010) are shown in Figure 4.

Major elements

All the analyzed Erongo whole-rock samples can be classified as subalkaline, peraluminous granites.

TABLE 3. REPRESENTATIVE EMP COMPOSITIONS OF TOURMALINE

wt.%	LH-7	LH-8	HG3-4	TB-1	TB-2	TB-3	TB-4	TB-5	TB-6	TB-7
SiO_2	36.54	36.45	35.45	35.45	35.48	35.51	35.53	35.40	35.43	36.54
TiO_2	0.04	0.08	0.10	0.35	0.37	0.41	0.21	0.23	0.11	0.21
Al_2O_3	36.42	36.22	36.56	32.50	32.48	32.39	32.57	32.50	32.45	36.51
B_2O_3(calc.)	10.61	10.59	10.52	10.28	10.30	10.29	10.30	10.27	10.26	10.59
FeO_t	11.99	11.39	11.35	15.28	15.31	15.35	15.31	15.38	15.33	9.18
MnO	bdl	bdl	bdl	0.06	0.05	0.04	0.05	0.04	0.04	0.09
MgO	0.02	0.12	0.24	0.29	0.30	0.27	0.26	0.23	0.30	0.34
ZnO	bdl	bdl	bdl	bdl	bdl	bdl	bdl	bdl	bdl	bdl
CaO	bdl	bdl	bdl	0.07	0.07	0.06	0.06	0.06	0.06	0.02
Na_2O	1.04	1.29	1.68	2.01	2.13	2.12	2.20	2.18	2.16	1.34
K_2O	bdl	0.01	0.04	0.03	0.03	0.04	0.04	0.04	0.03	0.02
Li_2O(calc.)	0.51	0.62	0.59	0.35	0.38	0.39	0.40	0.38	0.37	0.84
H_2O(calc.)	3.58	3.53	3.53	3.15	3.18	3.20	3.14	3.10	3.13	3.50
F	0.18	0.26	0.22	0.83	0.78	0.75	0.87	0.95	0.86	0.33
F ≡ O	–0.08	–0.11	–0.09	–0.35	–0.33	–0.31	–0.37	–0.40	–0.36	–0.14
Total	100.87	100.45	100.17	100.29	100.53	100.50	100.56	100.35	100.15	99.38
apfu										
Na	0.331	0.411	0.538	0.657	0.698	0.694	0.720	0.715	0.708	0.428
Ca	bdl	bdl	bdl	0.013	0.012	0.011	0.010	0.011	0.010	0.004
K	bdl	0.003	0.008	0.007	0.006	0.009	0.009	0.008	0.006	0.005
Vac(calc.)	0.669	0.586	0.454	0.323	0.284	0.286	0.261	0.266	0.276	0.564
Σ X	1.000	1.000	1.000	1.000	1.000	1.000	1.000	1.000	1.000	1.000
Fe	1.642	1.564	1.567	2.161	2.161	2.167	2.161	2.177	2.173	1.260
Mg	0.005	0.028	0.058	0.073	0.076	0.069	0.064	0.059	0.076	0.084
Al	1.012	0.990	0.969	0.471	0.450	0.441	0.472	0.469	0.479	1.063
Mn	bdl	bdl	bdl	0.008	0.006	0.006	0.006	0.006	0.005	0.012
Li(calc.)	0.335	0.407	0.392	0.241	0.259	0.264	0.269	0.260	0.253	0.554
Zn	bdl	bdl	bdl	bdl	bdl	bdl	bdl	bdl	bdl	bdl
Ti	0.005	0.010	0.013	0.044	0.046	0.052	0.027	0.029	0.013	0.026
Σ Y	2.999	2.999	2.999	2.998	2.999	3.000	3.000	3.000	3.000	3.000
Al	6.000	6.000	6.000	6.000	6.000	6.000	6.000	6.000	6.000	6.000
Σ Z	6.000	6.000	6.000	6.000	6.000	6.000	6.000	6.000	6.000	6.000
Si	5.984	5.984	5.854	5.994	5.989	5.995	5.996	5.989	6.004	5.999
Al	0.016	0.016	0.146	0.006	0.011	0.005	0.004	0.011	0.000	0.001
Σ T	6.000	6.000	6.000	6.000	6.000	6.000	6.000	6.000	6.004	6.000
B(calc.)	3.000	3.000	3.000	3.000	3.000	3.000	3.000	3.000	3.000	3.000
H(calc.)	3.907	3.867	3.887	3.554	3.585	3.602	3.533	3.494	3.541	3.827
F	0.093	0.133	0.113	0.446	0.415	0.398	0.466	0.506	0.459	0.172
Σ W+V	4.000	4.000	4.000	4.000	4.000	4.000	4.000	4.000	3.999	4.000
species	*foitite*	*foitite*	*schorl*	*schorl*	*schorl*	*schorl*	*F-schorl*	*schorl*	*schorl*	*foitite*

Bi, Cr, V, and Pb analyzed for but not detected; *apfu* calculated based on 31 anions per formula unit; H, B, and Li calculated by stoichiometry; bdl = below detection limit.

There is a slight separation in peraluminosity between HG and Trumbull *et al*. (2008) samples compared to those from LH. Overall, the Erongo Granite is aluminum-rich, consistent with the presence of muscovite, topaz, and garnet as accessory phases in some whole-rock samples.

The HG samples have a consistently higher FeO_T/MgO ratio compared to those from LH, as can be seen in Figure 16, suggesting different source contributions to the magmas from these two localities. The calc-alkaline affinity of LH samples is consistent with the high Mg-enrichment in LH biotite samples.

Trace elements

The geochemical distinction between the two localities, HG and LH, is clearly shown in Figures

TABLE 3. CONTINUED.

wt.%	HG3-1	HG3-3	HG3-4	HG3-5	HG3-7	HG3-8	LH-1	LH-3	LH-5	LH-6
SiO_2	34.70	34.66	34.70	34.59	35.68	35.69	35.34	35.41	36.45	35.23
TiO_2	0.27	0.31	0.27	0.33	0.67	0.64	bdl	0.18	0.08	0.08
Al_2O_3	33.56	33.66	33.56	33.67	31.34	31.40	34.54	32.59	36.22	36.50
B_2O_3(calc.)	10.22	10.30	10.28	10.30	10.32	10.33	10.29	10.26	10.50	10.52
FeO_t	14.62	14.68	14.62	14.66	14.06	14.16	13.95	15.30	11.39	11.69
MnO	0.01	0.03	0.01	0.02	0.08	0.08	0.03	0.08	bdl	bdl
MgO	0.22	0.24	0.22	0.28	2.11	2.14	bdl	0.17	0.12	0.34
ZnO	bdl	bdl	bdl	bdl	bdl	0.01	bdl	bdl	bdl	bdl
CaO	0.28	0.33	0.28	0.26	0.19	0.17	bdl	0.11	bdl	bdl
Na_2O	2.11	2.11	2.11	2.21	2.12	2.06	1.57	2.04	1.29	1.88
K_2O	0.03	0.02	0.03	0.03	0.03	0.03	0.06	0.01	0.01	0.02
Li_2O(calc.)	0.03	0.42	0.42	0.41	0.26	0.22	0.03	0.03	0.03	0.55
H_2O(calc.)	3.20	3.23	3.21	3.28	3.12	3.11	3.07	3.34	3.50	3.43
F	0.70	0.68	0.70	0.59	0.92	0.95	1.01	0.39	0.26	0.41
F ≡ O	–0.29	–0.29	–0.29	–0.25	–0.39	–0.40	–0.43	–0.17	–0.11	–0.17
Total	99.68	100.38	100.13	100.37	100.49	100.59	99.89	99.75	99.85	100.48
apfu										
Na	0.695	0.691	0.691	0.724	0.690	0.670	0.514	0.674	0.414	0.603
Ca	0.051	0.060	0.051	0.046	0.034	0.031	bdl	0.020	bdl	bdl
K	0.006	0.005	0.006	0.005	0.005	0.007	0.013	0.003	0.003	0.003
Vac(calc.)	0.248	0.244	0.252	0.224	0.270	0.291	0.473	0.302	0.583	0.394
Σ X	1.000	1.000	1.000	1.000	1.000	1.000	1.000	1.000		1.000
Fe	2.079	2.071	2.068	2.069	1.979	1.992	1.970	2.177	1.566	1.614
Mg	0.056	0.060	0.056	0.071	0.530	0.538	bdl	0.044	0.028	0.083
Al	0.621	0.541	0.553	0.535	0.218	0.227	0.845	0.536	1.062	0.925
Mn	0.002	0.004	0.002	0.003	0.011	0.011	0.004	0.011	bdl	bdl
Li(calc.)	0.024	0.283	0.286	0.277	0.177	0.150	0.021	0.021	0.021	0.368
Zn	bdl	bdl	bdl	bdl	bdl	0.001	bdl	bdl	bdl	bdl
Ti	0.035	0.040	0.035	0.042	0.084	0.081	bdl	0.023	0.010	0.010
Σ Y	2.816	3.000	3.000	2.999	3.000	3.000	2.841	2.811	3.000	2.999
Al	6.000	6.000	6.000	6.000	6.000	6.000	6.000	6.000	6.000	6.000
Σ Z	6.000	6.000	6.000	6.000	6.000	6.000	6.000	6.000	6.000	6.000
Si	5.898	5.848	5.867	5.837	6.007	6.006	5.969	6.021	6.031	5.819
Al	0.102	0.152	0.133	0.163	0.000	0.000	0.031	0.000	0.016	0.181
Σ T	6.000	6.000	6.000	6.000	6.007	6.006	6.000	6.000	6.000	6.000
B(calc.)	3.000	3.000	3.000	3.000	2.999	2.999	3.000	3.000	3.000	3.000
H(calc.)	3.628	3.638	3.626	3.688	3.508	3.496	3.459	3.788	3.863	3.785
F	0.376	0.362	0.374	0.312	0.492	0.503	0.539	0.211	0.134	0.215
Σ W+V	4.000	4.000	4.000	4.000	3.999	3.999	4.000	4.000	4.000	4.000
species	*schorl*	*schorl*	*schorl*	*schorl*	*schorl*	*F-schorl*	*F-schorl*	*schorl*	*foitite*	*schorl*

Bi, Cr, V, and Pb analyzed for but not detected; *apfu* calculated based on 31 anions per formula unit; H, B, and Li calculated by stoichiometry; bdl = below detection limit.

17–19. Whole-rock samples of the Erongo Granite are cerium-rich, with a ratio of approximately 50–55% Ce/(Ce + La + Nd) consistent with the presence of "allanite", "monazite", and "bastnäsite" in samples from nearly all locations. There is a slight separation of LH granite samples from the others, having roughly 10% more La/(Ce + La + Nd) and/or 10% less Nd/(Ce + La + Nd). In addition, there is separation between HG and LH samples with respect to Ce, La, and Y. The LH samples are cerium-dominant, whereas the HG samples are slightly yttrium-dominant. "Xenotime" is much more abundant in samples from HG compared to those from LH.

Relative to Ta and Nb, both LH and HG granite are enriched in Ti. Niobium and Ta concentrations are very low. There is a small difference in Ti between the LH and HG areas. Titanite, ilmenite–pyrophanite, and very small grains of TiO_2 minerals were found in

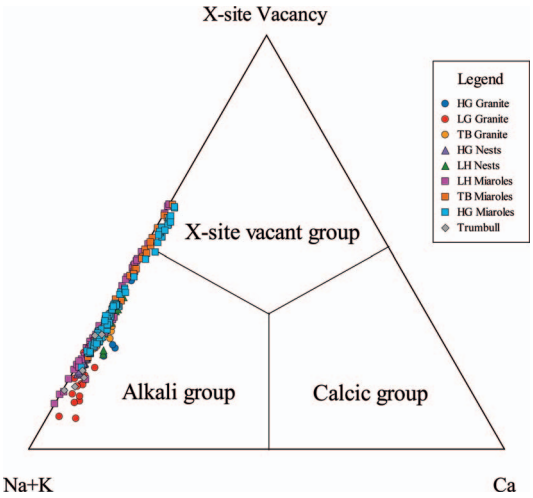

FIG. 10. Tourmaline X-site (Na + K) – Ca – (X-site vacancy) ternary plot showing the trend of Erongo tourmaline from alkali dominant tourmaline to slightly X-site vacant. Tourmaline from granite and TN are all alkali rich. Some miarolitic tourmaline extends into the X-site vacant field. All are very low in Ca.

appreciable amounts from the LH area but were rare to absent in HG samples. Niobium and Ta are only present in small amounts in both areas, with Nb > Ta.

The HG and LH samples can be differentiated with respect to REE with the chondrite-normalized REE plot shown in Figure 17. The LH samples are LREE-enriched over HREE. The HG samples are distinctly enriched in HREE compared to those from LH, but there is only a slight enrichment of LREE over HREE. These patterns are consistent with the presence of "allanite", which is exclusive to LH samples, whereas HREE-bearing "xenotime" is relatively enriched in HG and TB.

The negative Eu-anomaly of the HG and some of the Trumbull samples is pronounced, suggesting these samples are highly evolved with respect to REEs. The LH samples and the remainder of the Trumbull samples have a less-pronounced negative Eu-anomaly, suggesting that they are less evolved. The deeper negative Eu-anomaly of the HG samples compared to that of the LH samples is in accordance with the lower modal percentages of plagioclase in HG.

The upper continental crust-normalized spider diagram of Taylor & McLennan (1985) is shown in Figure 18. Relative to the upper continental crust, there are pronounced geochemical differences between the LH and HG whole-rock samples. The HG granite is

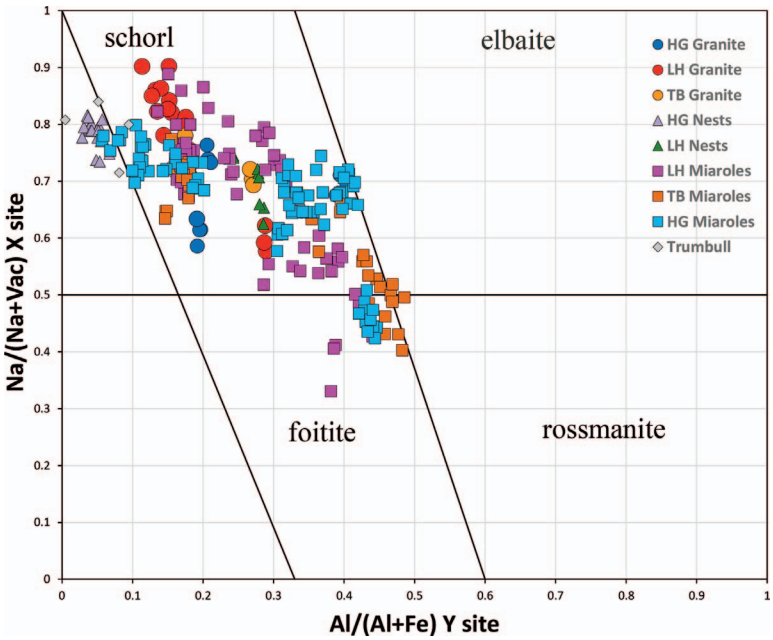

FIG. 11. Plot of Na/(Na + Vac) *versus* Al/(Al + Fe) composition of Erongo tourmaline showing the fields for schorl, foitite, elbaite, and rossmanite. Compositions range from Fe-rich schorl to low-Fe schorl and to foitite. The Li content of Erongo tourmaline is too low for elbaite or rossmanite.

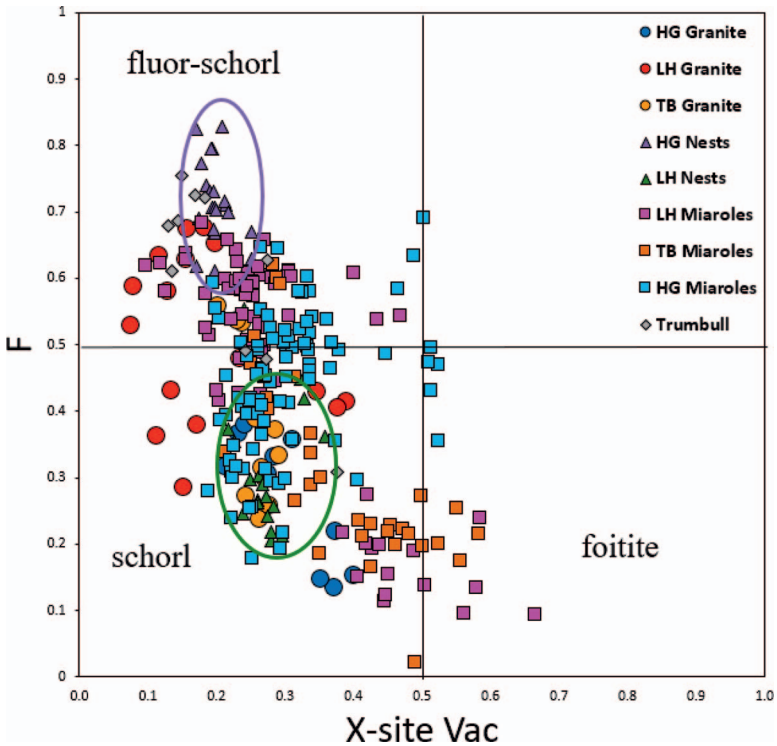

FIG. 12. Fluorine *versus* X-site vacancy plot of all Erongo tourmaline showing tourmaline compositions ranging from F-rich fluor-schorl through OH-rich schorl to slightly X-site vacant foitite. Note that tourmaline from HG TN is the highest in fluorine, all plotting as fluor-schorl. Tourmaline from LH TN is all schorl. Fields of TN compositions are encircled: the purple oval is HG TN, the green is LH TN.

more enriched in Cs, Rb, U, Ta, Sm, and HREE than the LH granite. The HG granite is more depleted in Ba, Sr, Zr, and Ti than the LH granite. Overall, HG is more chemically evolved than the LH granite and the samples of Trumbull *et al*. (2010) are distributed in between. It is clear that there were strong chemical heterogeneities in different portions of the Erongo granitic melt.

Tectonic discrimination diagrams

A plot of Zr *versus* Ga/Al (Whalen *et al*. 1987) for the Erongo Granite samples fall in the A-type field (Boudreaux 2014). The HG samples plot completely within the A-type field, whereas the LH samples overlap the boundary between A-type or I&S-types. Granite samples from Pirajno (1990) plot completely within the A-type field. The anorogenic classification of the HG samples from the Zr/(10^4Ga/Al) plot is consistent with the high FeO_t/MgO ratio, the high K_2O concentration, and the anorogenic tectonic setting during the reported 132–134 Ma emplacement age in Wigand *et al*. (2004).

Pearce *et al*. (1984) tectonic discrimination diagrams (Fig. 19) show the distinct geochemical differences between HG and LH samples. Samples from HG can be classified as dominantly WPG, whereas those from LH are anomalous and appear to be syn-COLG.

Both trace element plots seem to imply that there are two distinct granites formed from different tectonic events. However, the Erongo granite samples are from a single intrusive event. Thus, some other explanation is required to reconcile the different trace element character between LH and HG.

DISCUSSION

Petrogenesis

The temporal, spatial, and broad geochemical relationships among the anorogenic igneous units in the Damara region are well established in the literature (Wigand *et al*. 2004, Haapala *et al*. 2007, Pirajno *et al*. 1990). During the Early Cretaceous the supercontinent Gondwana was in the initial stage of a massive rifting

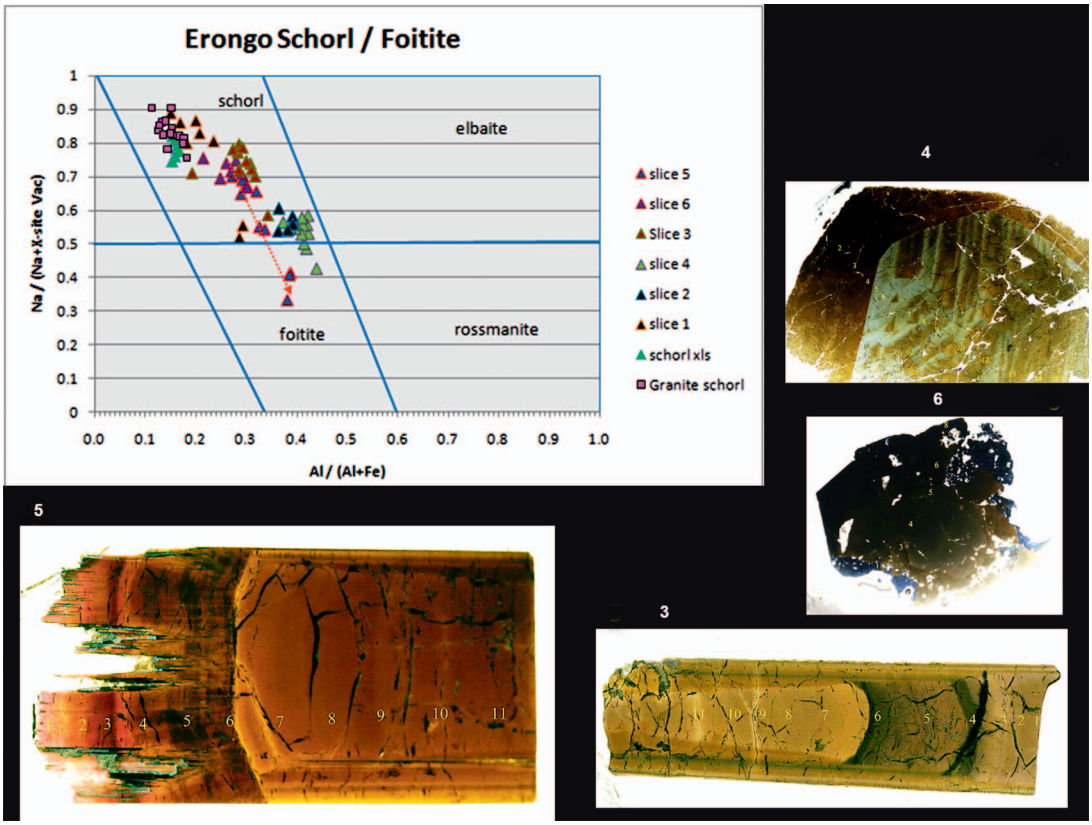

FIG. 13. Thin sections of tourmaline showing internal zonation. Compositional ranges in terms of Al/(Al + Fe) *versus* Na/(Na + vac) are shown on the plot. Compared to tourmaline from granite, the miarolitic tourmaline is richer in vacancy and lower in Fe. The red arrow shows the change in composition along crystal #5, from schorl to foitite. This image illustrates how the fibrous ends of crystals tend toward foitite compositions.

event. The western Gondwanan crust was subjected to tensional stress by the upwelling Tristan da Cunha mantle plume, eventually rifting the supercontinent and separating the land mass into Africa and South America by opening the Atlantic basin (Haapala *et al.* 2007). The ages reported in Wigand *et al.* (2004) for the Erongo anorogenic caldera complex fall within this time period (129–134.4 Ma).

Overall, tectonic discrimination of the Erongo Granite using whole-rock trace element geochemistry is consistent with an anorogenic tectonic setting. However, mineralogically and geochemically, the Erongo Granite is far from being a classic anorogenic rock. There is variability in modal proportions of the common rock-forming minerals, and trace-element concentrations span wide ranges, as shown by the chondrite-normalized REE and spider diagrams (Figs. 17–19). Minerals with stoichiometric titanium like titanite, rutile, and ilmenite–pyrophanite are ubiqui-

FIG. 14. Aquamarine from the Erongo Mountains. Representative prismatic specimen with pinacoid. Minor corroded orthoclase is attached (4 cm).

TABLE 4. REPRESENTATIVE EMP COMPOSITIONS OF BERYL

wt.%	HG-1brl	HG-7brl	HG-9brl	HG-17brl	LH-brl	LH-SP1brl
SiO_2	66.10	65.87	65.89	66.01	65.88	65.93
TiO_2	bdl	bdl	bdl	bdl	bdl	0.01
Al_2O_3	18.89	18.95	18.84	18.89	18.80	18.89
Sc_2O_3	bdl	bdl	bdl	0.01	0.01	0.02
BeO(calc.)	13.81	13.80	13.77	13.82	13.76	13.80
FeOt	0.10	0.26	0.16	0.34	0.10	0.22
MnO	bdl	bdl	bdl	bdl	bdl	0.01
CaO	0.02	bdl	bdl	bdl	bdl	bdl
Na_2O	0.13	0.31	0.22	0.31	0.21	0.26
K_2O	0.02	0.03	0.03	0.02	0.02	0.02
Total	99.07	99.22	98.92	99.40	98.80	99.16
apfu						
Be(calc.)	3.000	3.000	3.000	3.000	3.000	3.000
Σ Be	3.000	3.000	3.000	3.000	3.000	3.000
Al	1.992	1.981	1.986	1.975	1.988	1.982
Fe	0.008	0.019	0.012	0.026	0.007	0.017
Sc	bdl	bdl	bdl	0.001	0.001	0.002
Mn	bdl	bdl	bdl	bdl	bdl	0.001
Ca	0.002	bdl	bdl	bdl	bdl	bdl
Σ Oct	2.002	2.000	1.998	2.002	1.997	2.001
Si	5.978	5.959	5.973	5.964	5.977	5.966
Al	0.022	0.041	0.027	0.036	0.023	0.033
Ti	bdl	bdl	bdl	bdl	bdl	0.001
Σ Tet	6.000	6.000	6.000	6.000	6.000	6.000
Na	0.023	0.055	0.039	0.055	0.037	0.045
K	0.002	0.004	0.003	0.002	0.003	0.002
Σ Chan	0.025	0.059	0.043	0.057	0.040	0.046

Cs, Rb, and Mg analyzed for but not detected; *apfu* calculated based on 18 anions per formula unit; Be calculated by stoichiometry; bdl = below detection limit.

tous in samples from the LH and absent in those from HG. It is unlikely that the process of fractional crystallization could produce such pronounced dissimilarities within the same magma body. The heterogeneity of the Erongo Granite suggests that either the magma generation was not from a homogenous source, or that the magma composition was significantly changed in a non-uniform manner. With such a strong case for rift-related petrogenesis, the best options to explain the mineralogical and geochemical heterogeneities are (1) derivation from an already heterogeneous source, *i.e.*, the Damaran metasediments, and/or (2) extensive crustal contamination from the Damaran metasediments during magmatic ascent and emplacement.

Contamination of the Erongo granitic melt could have been introduced as the magma ascended through the Damara metasedimentary sequence. The Erongo complex and its sister intrusives were all emplaced within the Damara orogenic belt, comprised primarily of metasedimentary rock and crisscrossed by massive faults, allowing for a relatively less-resistant pathway for magma intrusion compared to the adjacent cratons. In fact, Aldrich (1986) was confident that the Erongo complex emplacement was related to the Omaruru Lineament, a large fault system separating the northern and southern portions of the Central Damaran Zone. Based on isotopic studies several authors have suggested that crustal contamination was a significant factor in developing the geochemical character of the Erongo Granite. Harris (1995) examined the oxygen isotopes ($\delta^{18}O$) of nine anorogenic units, including Erongo, and found evidence for higher $\delta^{18}O$ values towards the central zone of the Damara orogen. He attributes this increase to a thicker crust and therefore longer travel distance for the plutons. The Erongo Granite has $\delta^{18}O_{magma}$ values that range from 10.1 to 11.0%, which Harris (1995) interprets as essentially a crustal melt. Similarly, neodymium and strontium isotopic studies conducted by Trumbull *et al*. (2000, 2004) suggest a strong isotopic relationship between the Erongo granitoids and the rocks of the Damara sequence. The Erongo granitoids show no obvious affinity for the mantle array or Pre-Damara basement,

TABLE 5. REPRESENTATIVE EMP COMPOSITIONS OF ILMENITE–PYROPHANITE

wt.%	LH-1-ip-1	LH-3-ip-1	LH-3-ip-9	LH-7-ip-1
SiO_2	0.03	0.02	0.03	0.05
TiO_2	50.32	50.99	50.51	50.70
Al_2O_3	0.04	0.05	0.06	0.03
FeO	22.21	29.98	26.55	24.33
MnO	27.44	18.87	22.88	24.78
MgO	bdl	bdl	bdl	bdl
CaO	bdl	bdl	bdl	bdl
Total	100.05	99.91	100.04	99.89
apfu				
Fe	0.474	0.638	0.566	0.518
Mn	0.592	0.407	0.494	0.535
Mg	bdl	bdl	bdl	bdl
Ca	bdl	bdl	bdl	bdl
Σ X	1.066	1.045	1.060	1.053
Ti	0.965	0.976	0.968	0.972
Al	0.001	0.001	0.002	0.001
Si	0.001	0.001	0.001	0.001
Σ Y	0.967	0.978	0.971	0.974

Nb and Ta analyzed for but not detected; bdl = below detection limit. Normalized on 3 O atoms.

TABLE 6. DCP ANALYSES OF REES IN MIAROLITIC CAVITY FLUORITE

ppm	HG-1 fl	HB-3 fl	HG-fl2	HG-fl3	HG-fl4	HG-fl5
La	25	21	25	25	21	34
Ce	49	57	53	44	37	75
Nd	34	33	34	35	36	45
Sm	15	25	24	13	10	26
Eu	1.3	1	1.7	10	9	2.2
Gd	6	5	7	7	6	7
Dy	12	13	12	13	9	12
Yb	21	24	22	23	19	23
Y	110	85	84	96	66	93

Elements analyzed outlined in box.

as do other geographically related anorogenic intrusives (*e.g.*, Gross Spitzkoppe), but instead plot completely within the field of the Damaran metasedimentary rocks (Haapala *et al*. 2007).

Taken together, the mineralogical, geochemical, and isotopic evidence for the Erongo Granite having been an essentially crustal melt cannot be ignored. A rifting and mantle-involved model is necessary to explain the more mafic rocks of the Erongo complex and its sister intrusives but is not necessary for the Erongo Granite. Any original mantle signature seems to have been overprinted to the point that it is scarcely recognizable.

The mineralogical and geochemical characteristics of LH samples suggest more significant crustal contamination than that observed from HG samples.

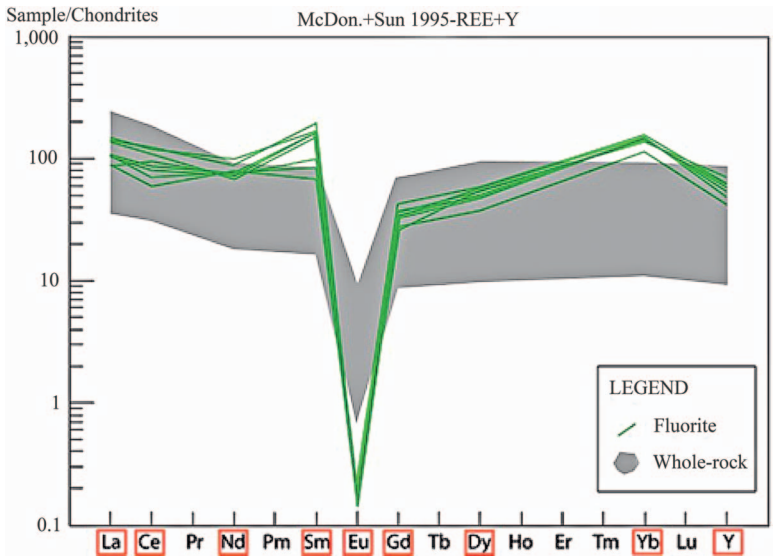

FIG. 15. Fluorite chondrite-normalized REE+Y diagram. CN values from McDonough & Sun (1995).

TABLE 7. COMPOSITE DATA SET OF WHOLE-ROCK ANALYSES *VIA* FUSION ICP-OES, ICP-MS, DCP, AND EMP

wt.%	LH-1	LH-3	LH-7	HG-1	HG-2	HG-3	HG-4
SiO_2	78.34	75.74	73.76	74.76	76.57	77.85	76.00
Al_2O_3	11.98	12.71	12.84	12.24	12.15	12.08	12.45
FeO_t	1.00	1.27	1.29	1.64	1.61	1.65	1.64
MnO	0.05	0.04	0.04	0.06	0.04	0.03	0.03
MgO	0.09	0.33	0.27	0.04	0.05	0.05	0.04
CaO	0.44	0.84	0.70	0.42	0.38	0.39	0.33
Na_2O	3.64	3.63	3.60	2.91	2.72	2.69	2.96
K_2O	4.46	4.37	4.90	5.17	4.91	5.30	5.16
TiO_2	0.12	0.22	0.26	0.08	0.08	0.10	0.07
P_2O_5	0.01	0.04	0.03	0.04	0.06	0.05	0.03
LOI	0.64	0.70	0.85	1.18	0.81	0.73	1.05
F	0.23	0.25	0.23	0.30	0.27	0.27	0.30
F = O	–0.10	–0.11	–0.10	–0.13	–0.11	–0.11	–0.13
Total	100.90	100.04	98.68	98.71	99.53	101.08	99.94
B	287	410	418	366	444	770	441
Li	198	240	212	23	27	132	182
Sc	2	2	2	5	6	5	6
Be	4	3	4	8	5	4	5
V	9	16	17	6	<5	5	5
Cr	<20	<20	<20	<20	<20	<20	<20
Co	<1	1	1	<1	<1	<1	<1
Ni	<20	<20	<20	<20	<20	<20	<20
Cu	<10	<10	<10	<10	<10	10	<10
Zn	<30	<30	<30	80	50	70	40
Ga	18	16	16	27	26	24	26
Ge	1.9	1.5	1.5	3.9	3	2.5	2.7
As	<5	<5	<5	24	11	22	12
Rb	169	139	130	790	906	688	849
Sr	14	89	65	8	7	13	6
Y	17.8	15.3	20.7	111	115	115	113
Zr	122	154	202	95	96	98	96
Nb	33.4	19.2	24.5	36.9	42.5	28.1	35.5
Mo	<2	<2	<2	<2	<2	<2	<2

This interpretation is based on the following observations: (1) the noticeably more calc-alkaline geochemistry (Fig. 16); (2) the lesser degree of geochemical evolution, based on a smaller negative europium anomaly (Fig. 17); (3) the less-pronounced negative barium anomaly (Fig. 18), as enrichment in barium has been widely attributed to a subducted sedimentary component following the work of Kay (1977, 1980); (4) the consistently LREE-enriched and HREE-depleted pattern of the LH samples (Fig. 17), which is very similar to the REE pattern of Andean continental arc rocks studied by Hildreth & Moorbath (1988), suggesting magmatic interaction with deep, garnet-bearing crust; (5) the tendency for whole-rock samples to plot within the I&S-type field in the Whalen *et al*. (1987) diagram and the VAG field in the tectonic discrimination diagrams of Pearce *et al*. (1984) (Fig. 19); and (6) the apparent higher oxygen fugacity of the original magma at the LH location, based on relatively higher magnetite abundance, a larger ferric iron component in biotites, and the presence of a titanite+magnetite+quartz assemblage.

Formation of miarolitic cavities and tourmaline-quartz orbicules

Fractional crystallization and fluid exsolution is interpreted to be the dominant mechanism by which the quartz-tourmaline orbicules and miarolitic cavities formed. During the crystallization of the highly contaminated and heterogeneous magma, volatile elements were excluded from the common rock-

TABLE 7. CONTINUED.

ppm	LH-1	LH-3	LH-7	HG-1	HG-2	HG-3	HG-4
Ag	0.6	0.7	0.9	0.6	<0.5	0.5	0.5
In	<0.1	<0.1	<0.1	0.1	0.1	0.1	0.1
Sn	2	2	2	38	50	33	32
Sb	<0.2	<0.2	<0.2	0.6	0.4	0.4	0.2
Cs	0.7	1.1	1	62.9	73.3	59.1	71.3
Ba	29	266	206	9	13	20	10
La	40.3	45.2	56.4	27.2	30.1	30.5	26.8
Ce	73	86.4	111	72.4	84.3	77.7	72.1
Pr	5.93	7.48	10.1	8.82	9.68	8.71	8.3
Nd	16.1	23.2	31	31.8	34.2	31	30
Sm	2.66	3.71	5.4	10.7	12.5	10.2	10.7
Eu	0.19	0.506	0.536	0.069	0.054	0.087	0.055
Gd	1.81	2.5	3.27	11.2	11.8	10.5	11.1
Tb	0.34	0.42	0.56	2.9	2.97	2.56	2.77
Dy	2.51	2.73	3.5	20.3	21.6	18.9	20.6
Ho	0.58	0.59	0.75	4.49	4.88	4.01	4.53
Er	2.03	1.82	2.25	14	14.7	12.7	14.2
Tm	0.35	0.276	0.35	2.09	2.23	1.91	2.09
Yb	2.75	1.84	2.41	13.5	14.5	12.1	13.6
Lu	0.518	0.3	0.397	1.94	2.08	1.76	1.97
Hf	4.4	4.1	5.4	4.3	4.6	3.8	4.4
Ta	2.94	1.53	2.11	5.22	7.34	4.24	6.18
W	<0.5	<0.5	<0.5	11	12.1	14.4	9.5
Tl	0.77	0.67	0.64	5.09	5.86	4.96	5.51
Pb	30	22	21	38	31	50	32
Bi	<0.1	0.2	<0.1	1.9	2.5	4.1	2
Th	32.7	19.4	23.1	41.2	40.3	36.3	38.4
U	3.51	2.34	2.62	49.7	8.38	37.1	7.09
Th/U	9.32	8.29	8.82	0.83	4.81	0.98	5.42
Nb/Ta	11.36	12.55	11.61	7.07	5.79	6.63	5.74
Zr/Hf	27.73	37.56	37.41	22.09	20.87	25.79	21.82
Y/Ho	30.69	25.93	27.60	24.72	23.57	28.68	24.94

forming minerals of a granitic system (quartz, orthoclase, and albite) and became increasingly concentrated in the remaining melt. The most abundant volatiles in the Erongo Granite system are F^{1-}, H_2O, and BO_3^{3-}, and the most important incompatible elements include Rb, Be, Nb, Zr, U, Th, and the REEs. Lithium usually behaves incompatibly in granitic systems but was found to be relatively compatible in Erongo biotite samples.

At some point during the increasing enrichment of volatiles in the fractionating melt, the silicate magma became oversaturated with volatiles and a second fluid phase exsolved. The quartz-tourmaline orbicules, visible in nearly all outcrops of the Erongo Granite, are thought to represent the initial stages of exsolution. The tourmaline, quartz, and a small amount of accessory minerals are proposed to have crystallized from a mixture of a borosilicate melt and a H_2O- and F-rich fluid in a manner similar to that described for the tourmaline orbicules of the Seagull Batholith in the Yukon Territory of Canada (Samson & Sinclair 1992). The abundance of quartz-tourmaline orbicules attests to an unusually high starting concentration of F^-, H_2O, and BO_3^{3-} in the granitic magma. In typical A-type granites, H_2O and especially BO_3^{3-} are uncommon volatile components. We infer extensive input from the Damara metasediments to explain the abundance of H_2O and BO_3. The rounded profiles of quartz-tourmaline orbicules in outcrop (Fig. 9) are likely inherited from the initial, bubble-like shape of pods of exsolved fluid. The high viscosity of the shallow-level silicate magma restricted the mobility of the small exsolved pods and caused many of them to crystallize essentially in place.

Miarolitic cavities are interpreted to have been created by the coalescence of pods of exsolved fluid

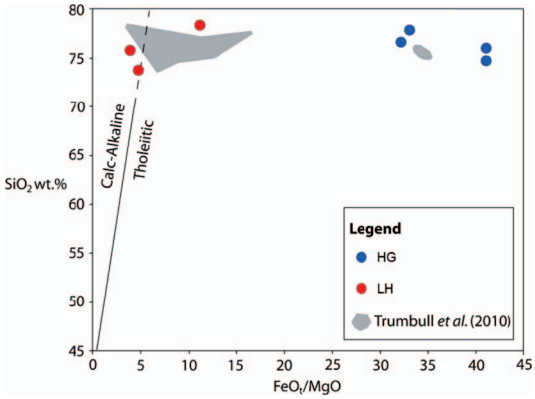

FIG. 16. Calc-alkaline *versus* Tholeiitic affiliation Miyashiro (1975) showing the higher FeO/MgO ratio of HG granites compared to LH.

and continued fractional crystallization. As such, both the tourmaline orbicules and miarolitic cavities are proposed to have an origin related to volatile exsolution. As small bubbles of exsolved fluid coalesced, the net buoyant force became stronger and overcame the viscosity of the silicate melt, causing the exsolved fluids to ascend toward the roof zone of the magma chamber. The upward migration was eventually arrested as the pods moved into the more viscous rapidly crystallizing roof zone. In the field, miarolitic cavities are not as ubiquitous as the tourmaline orbicules but are concentrated in higher areas. During ascent, larger pods of silicate fluid captured and incorporated any exsolved fluids in their paths. Since the magma body is thought to have been heterogeneous because of non-uniform contamination, input from different parts of the magma may have been important in changing the geochemical composition of the ascending fluids.

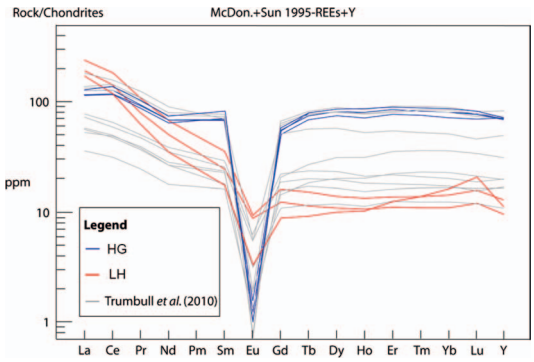

FIG. 17. Chondrite-normalized REE+Y diagram. CN values from McDonough & Sun (1995).

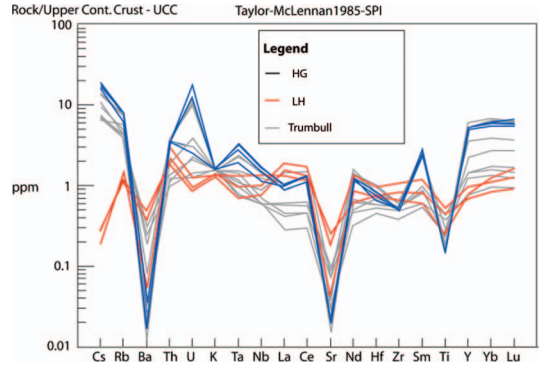

FIG. 18. Upper continental crust-normalized spider diagram of Taylor & McLennan (1985).

Changes in fluid chemistry were likely also induced by continued fractional crystallization. The boron content of the melt increases the solubility of H_2O in the melt (Simmons *et al*. 2012). The removal of B by the crystallization of tourmaline promotes further exsolution of H_2O, which contributes to the formation of the miarolitic cavities (Simmons *et al*. 2012). Tourmaline and topaz have the highest H_2O contents in miarolitic cavity samples, supporting the idea that the fluids became more aqueous during evolution. Abundant fluor-schorl and accessory fluorite and topaz in TN samples suggest that F was slightly more elevated than OH in the early mineralization of the exsolved fluids. At the miarolitic cavity stage fractional crystallization concentrated Be sufficiently for the crystallization of beryl. Beryl was found exclusively in the miarolitic cavities and contains numerous fluid inclusions. Overall Li content appears to have been low and, as Li is relatively compatible in earlier crystallized mica, it never became concentrated enough to form Li minerals. During miarolitic cavity formation, the exsolved fluids were so enriched in volatiles that the coupling of rapid diffusion rates and low nucleation rates produced pegmatitic textures with few, large, and well-formed crystals. In areas of HG granite, the abundance of miarolitic cavities is remarkable. Viewed from a distance the exposed eastern cliff face of HG looks like Swiss cheese.

Evolutionary model

The following evolutionary model is proposed for the generation of the Erongo Granite and its boron-rich quartz-tourmaline orbicules and miarolitic cavities:

(a) During the late Proterozoic and early Cambrian, tectonic convergence between the Congo and Kalahari cratons produced the Damara orogenic

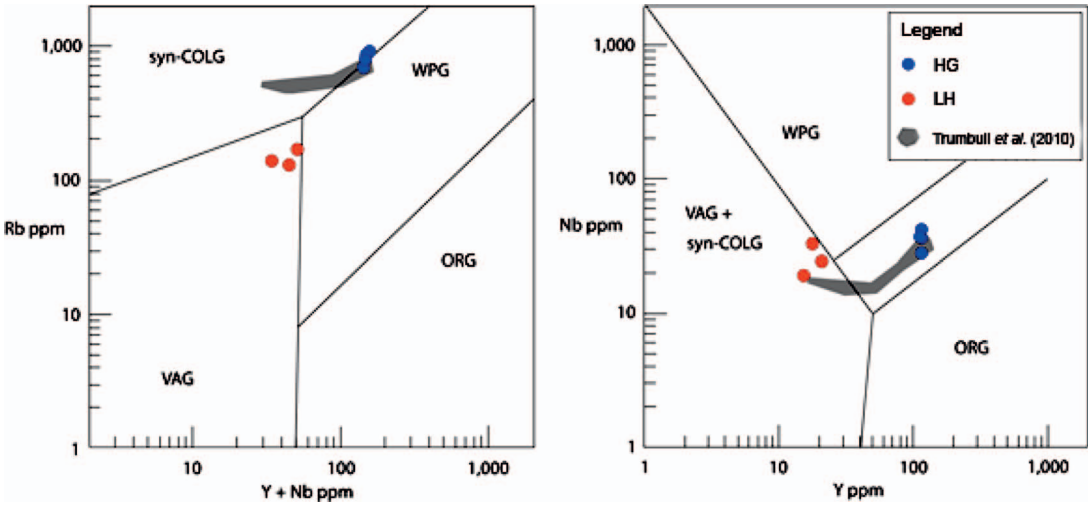

FIG. 19. Tectonic discrimination diagrams of Pearce *et al.* (1984).

zone. Volcanic arc I-type plutons were produced during the subduction of the oceanic lithosphere beneath the Congo craton. Upon collision of the continental masses, sedimentary rocks were extensively metamorphosed and orogenic, S-type plutons were emplaced.

(b) By the early Cretaceous, the Damara orogen had been heavily eroded, exposing deeper metamorphic facies. The Tristan da Cunha mantle plume upwelled under the western portion of the Gondwana supercontinent, putting the crust in tension. Thermal energy from the mantle plume and decompression caused partial melting of the upper mantle and deep continental crust. The resulting melts were highly tholeiitic and propagated up to the surface along pre-existing structural weaknesses from the Damara orogen (*e.g.*, Omaruru Lineament) and possibly along normal faults associated with the new tensional stress regime. These melts eventually broke the surface and deposited massive flood basalts.

(c) The Namibian crust was subjected to less heat and tension as the initial surge of thermal energy from the mantle plume dwindled and a successful continental rift was finally established that evolved into the Mid-Atlantic Ridge. Under these new pressure and temperature conditions, the high-temperature minerals of the upper mantle could not be melted, and the primary location of magmatic sourcing gradually moved from the upper mantle and deep crust to the middle crust.

(d) The Erongo felsic magma was generated primarily in the lower crust with a small amount of input from the upper mantle. The melt intruded upward along the Omaruru Lineament and was heavily contaminated by the rocks of the Damara sequence. Volatiles and incompatible elements were readily incorporated into the melt.

(e) The magma was shallowly emplaced beneath a tholeiitic basalt and caused doming of the surface. Crystallization began to take place rather quickly, producing granodiorite masses. Fractional crystallization caused the remaining melt to become more felsic. During crystallization of the granodiorite, small fractures allowed the magma to vent and deposit rhyodacite tuffs.

(f) Withdrawal of fluid from the magma chamber *via* volcanic events eventually led to the collapse of the complex and the formation of a caldera. The remaining melt intruded around the periphery of the complex along newly created normal faults.

(g) Emplacement of the granitic magma at shallower depths caused an increase in the rate of crystallization. The volatile content, which was already high to begin with, became so large that the silicate magma exsolved a second fluid phase. Small pods of exsolved fluid interacted with the remaining melt and crystallized in place to become quartz-tourmaline orbicules. Some exsolved pods coalesced into larger structures and were able to buoyantly ascend through the viscous silicate melt. During ascension, they swept up smaller pods of exsolved fluid and continued to undergo fractional crystallization. These two processes eventually led to a more evolved geochemical

composition in some miarolitic cavities, where beryl is a common mineral, tourmaline compositions trend toward foitite and rossmanite, and rare jeremejevite is found. The extremely high proportion of volatiles in the miarolitic cavities allowed for the development of pegmatitic texture and euhedral crystals.

Conclusion

The Erongo Granite is an early Cretaceous rift-related granite that has mineralogical and geochemical characteristics that do not strictly adhere to classic anorogenic systems. In the field, quartz-tourmaline orbicules and miarolitic cavities that host abundant boron mineralization are observed, which is unusual for granites related to zones of continental rifting. Lithium is slightly enriched in the Erongo Granite and is primarily accommodated by micas; consequently, there is insufficient Li to form Li minerals. Similarly, significant H_2O enrichment is generally not encountered in anorogenic granites. Geochemical investigations of topaz and tourmaline revealed that water was important in the formation of late-stage tourmaline nests and miarolitic cavities, as H_2O became increasingly concentrated in the melt by fractional crystallization and eventually exsolved from the silicate magma.

From a bulk geochemical perspective, the Erongo Granite has an overall geochemical character that is more like the Damaran metasediments than the pre-Damara basement or mantle. As a result, tectonic discrimination diagrams give overlapping signatures for the clearly anorogenic Erongo Granite. Oxygen, neodymium, strontium, and boron isotopic studies (Harris 1995, Trumbull *et al*. 2000, 2004) all point to substantial input from the metasedimentary rocks of the Damara orogen, either from direct sourcing or extensive contamination during magmatic ascent and emplacement.

Thus, an initial rift-related evolutionary model for the Erongo Granite followed by significant crustal input from the Damaran metasediments to yield the hybrid anorogenic-orogenic geochemistry and mineralogy is consistent with our findings. The petrogenesis of the quartz-tourmaline orbicules and NYF-type miarolitic pegmatites is closely related to the parental granite so that the pegmatites reflect the contaminated nature of the granite. This atypical geochemistry with elevated H_2O, B, and Li is more enhanced in the pegmatites, where fractional crystallization has accumulated the volatile and incompatible elements to the point where significant changes in mineralogy are observed.

Acknowledgments

We are indebted to the Maine Mineral & Gem Museum and the Department of Earth and Environmental Sciences at the University of New Orleans for their support of the analytical facilities. We are indebted to numerous artisanal miners from the Erongo mountain area who generously gave assistance in accessing producing areas on the mountain and provided samples for analysis. We gratefully acknowledge constructive reviews by two anonymous reviewers who helped improve the manuscript. The editorial assistance of Lee Groat is gratefully acknowledged.

References

Aldrich, S. (1986) Progress report on a gravity and magnetic investigation of the Messum and Erongo igneous complexes. *Communications of the Geological Survey of South West Africa/Namibia* **2**, 47–52.

Blümel, W.D., Emmermann, R., & Hüser, K. (1979) *Der Erongo: geowissenschaftliche Beschreibung und Deutung eines südwestafrikanischen Vulkankomplexes*. Scientific Research Series, S.W. African Scientific Society **16**, 140 pp.

Boudreaux, A. (2014) *Mineralogy and geochemistry of the Erongo Granite and interior quartz-tourmaline orbicules and NYF-type miarolitic pegmatites, Namibia*. University of New Orleans Theses and Dissertations, Paper 1854, 246 pp.

Bowden, P., Kinnaird, J.A., Diehl, M., & Pirajno, F. (1990) Anorogenic granite evolution in Namibia—a fluid contribution. *Geological Journal* **25**, 381–390.

Cairncross, B. & Bahmann, U. (2006) Famous mineral localities: The Erongo Mountains, Namibia. *Mineralogical Record* **37**, 361–370.

Camp, K.F. (2011) *Mineralogy and Geochemistry of Anorogenic Miarolitic Pegmatites Associated with the White Mountain Intrusive Suite, New Hampshire Pegmatites of the Moat Mountain*. University of New Orleans Theses and Dissertations, Paper 1363, 120 pp.

Cloos, H. (1911) Geologische Beobachtungen in Südafrika II. Geologie des Erongo im Hererolande. *Beiträge zur geologischen Erforschung der Deutschen Schutzgebiete* **3**, 84 pp.

Cloos, H. (1919) Der Erongo – ein vukanisches Massiv im Tafelgebirge des Hererolandes und seine Bedeutung fuer die Raumfrage plutonischer Massen. *Beitraege zur geologischen Erforschung der Deutschen Schutzgebiete* **17**, 238 pp.

Emmermann, R. (1979) Aufbau und Entstehung des Erongo-Komplexes. Der Erongo. Geowissenschaftliche Beschreibung und Deutung eines südwestafrikanischen Vulkankomplexes, Windhoek. *Southwest African Scientific Society* **16**, 16–53.

Haapala, I., Frindt, S., & Kandara, J. (2007) Cretaceous Gross Spitzkoppe and Klein Spitzkoppe stocks in Namibia: Topaz-bearing A-type granites related to continental rifting and mantle plume. *Lithos* **97**, 174–192.

Harris, C. (1995) Oxygen isotope geochemistry of the Mesozoic anorogenic complexes of Damaraland, northwest Namibia: Evidence for crustal contamination and its effect on silica saturation. *Contributions to Mineralogy and Petrology* **122**, 308–321.

Hildreth, W. & Moorbath, S. (1988) Crustal contributions to arc magmatism in the Andes of central Chile. *Contributions to Mineralogy and Petrology* **98**, 455–489.

Kay, R.W. (1977) Geochemical constraints on the origin of Aleutian magmas. *In* Island Arcs, Back-arc Basins, and Deep-sea Trenches **1** (M. Talwani & W.C. Pittman III, eds.). American Geophysical Union, Maurice Ewing Series, Washington, D.C., United States (229–242).

Kay, R.W. (1980) Volcanic arc magmas: implications of a melting-mixing model for element recycling in the crust-upper mantle system. *Journal of Geology* **88**, 497–522.

McDonough, W.F. & Sun, S.S. (1995) The Composition of the Earth. *Chemical Geology* **120**, 223–253.

Miyashiro, A. (1975) Classification, characteristics, and origin of ophiolites. *Journal of Geology* **83**, 249–281.

Pearce, J.A., Harris, N.B., & Tindle, A.G. (1984) Trace element discrimination diagrams for the tectonic interpretation of granitic rocks. *Journal of Petrology* **25**, 956–983.

Pirajno, F. (1990) Geology, geochemistry and mineralisation of the Erongo Volcanic Complex, Namibia. *South African Journal of Geology* **93**, 485–504.

Pouchou, J.L. & Pichoir, F. (1991) Quantitative analysis of homogeneous or stratified microvolumes applying the model "PAP" in microprobe analysis. *In* Electron Probe Quantification (K.F.J. Heinrich & D.E. Newbury, eds.). Plenum Press, New York City, New York, United States (31–75).

Rieder, M., Cavazzini, G., D'Yakonov, Y., Frank-Kamenetskii, V.A., Gottardi, G., Guggenheim, S., Koval, P.V., Muller, G., Neiva, A.M.R., Radoslovich, E.W., Robert, J.L., Sassi, F.P., Takeda, H., Weiss, Z., & Wones, D.R. (1998) Nomenclature of the micas. *Canadian Mineralogist* **36**, 41–48.

Samson, I.M. & Sinclair, W.D. (1992) Magmatic hydrothermal fluids and the origin of quartz-tourmaline orbicules in the Seagull batholith, Yukon Territory. *Canadian Mineralogist* **30**, 937–954.

Schneider, G. (2004) *The roadside geology of Namibia 97*. Gebr. Borntraeger, Berlin, Germany.

Selway, J.B., Černý, P., Hawthorne, F.C., & Novák, M. (2000) The Tanco pegmatite at Bernic Lake, Manitoba, Canada. XIV. Internal tourmaline. *Canadian Mineralogist* **38**, 877–891.

Simmons, W.B., Pezzotta, F., Shigley, J.E., & Beurlen, H. (2012) Granitic pegmatites as sources of colored gemstones. *Elements* **8**, 281–287.

Simmons, W.B., Falster, A.U., Webber, K.L., Roda-Robles, E., Boudreaux, A.P., Grassi, L.R., & Freeman, G. (2016) Bulk composition of Mt. Mica pegmatite, Maine, USA: Implications for the origin of an LCT type pegmatite by anatexis. *Canadian Mineralogist* **54**, 1053–1070.

Taylor, S.R. & McLennan, S.M. (1985) *The continental crust: Its composition and evolution*. Blackwell Scientific Publications, Oxford, England, 312 pp.

Tischendorf, G., Gottesmann, B., Forster, H.-J., & Trumball, R.B. (1997) On Li-bearing micas: Estimating Li from electron microprobe analyses and an improved diagram for graphical representation. *Mineralogical Magazine* **61**, 809–834.

Trumbull, R.B., Emmermann, R., Bühn, B., Gerstenberger, H., Mingram, B., Schmitt, A., & Volker, F. (2000) Insights on the genesis of the Cretaceous Damaraland igneous complexes in Namibia from a Nd-and Sr-isotopic perspective. *Communications of the Geological Survey of Namibia* **12**, 313–324.

Trumbull, R.B., Harris, C., Frindt, S., & Wigand, M. (2004) Oxygen and neodymium isotope evidence for source diversity in Cretaceous anorogenic granites from Namibia and implications for A-type granite genesis. *Lithos* **73**, 21–40.

Trumbull, R.B., Krienitz, M.S., Gottesmann, B., & Wiedenbeck, M. (2008) Chemical and boron-isotope variations in tourmalines from an S-type granite and its source rocks: The Erongo Granite and tourmalinites in the Damara Belt, Namibia. *Contributions to Mineralogy and Petrology* **155**, 1–18.

Trumbull, R.B., Förster, H., & Rhede, D. (2010) REE-Y-Th-U-bearing accessory minerals and their contribution to the lanthanide and actinide trace-element budget in an anorogenic granite from the Erongo Complex, NW Namibia. *Zeitschrift für Geologische Wissenschaften* **38**, 145–165.

von Bezing, L., Bode, R., & Jahn, S. (2007) *Namibia Minerals and Localities*. Bode Verlag GmbH, 856 pp.

Whalen, J.B., Currie, K.L., & Chappell, B.W. (1987) A-type granites: geochemical characteristics, discrimination and petrogenesis. *Contributions to Mineralogy and Petrology* **95**, 407–419.

Wigand, M., Schmitt, A.K., Trumbull, R.B., Villa, I.M., & Emmermann, R. (2004) Short-lived magmatic activity in an anorogenic subvolcanic complex: $^{40}Ar/^{39}Ar$ and ion microprobe U–Pb zircon dating of the Erongo, Damaraland, Namibia. *Journal of Volcanology and Geothermal Research* **130**, 285–305.

WILSON, A.D. (1955) A new method for the determination of ferrous iron in rocks and minerals. *Bulletin of the Geological Survey of Great Britain* **9**, 56–58.

Received December 5, 2017. Revised manuscript accepted June 4, 2018.

APPENDIX 1

METHODS

Heavy mineral separation

Rock fragments were crushed in a SPEX 4200 Jaw Crusher® and screened through a No. 20 mesh (0.841 mm) and then density separated using lithium metatungstate solution with a density of 3.1 g/cm^3.

Scanning electron microscopy

An AMRAY 1820 Digital Scanning Electron Microscope (SEM) was employed in this study. Samples were polished and coated with 250 Å carbon. The instrument was operated under an acceleration potential of 20 kV. The IXRF Systems Inc. software was used to collect images, spectra, and X-ray maps.

Electron microprobe analysis

Samples were analyzed quantitatively with an ARL-SEMQ Electron Microprobe (EMP) using Wavelength Dispersive Spectroscopy (WDS) under an acceleration potential of 15 kV and a beam current of 15 nA. A 2 μm beam diameter was used in the analyses and count times were 45 s per spot.

Standards used include: adularia, Fibbia (K); albite, Tiburon (Na); andalusite, Minas Gerais (Al, Si); synthetic $Bi_4Ge_3O_{12}$, (Bi); chromite, Stillwater, Montana (Cr); clinopyroxene, "Cpx-26"(Ca, Fe, Mg, Ti); "fluortopaz", Thomas Range, Utah (F); synthetic PbO (Pb); rhodonite, Broken Hill (Mn); synthetic TiO_2 (TiO_2); synthetic V_2O_5 (V); synthetic ZnO (Zn). Other MAN standards used in addition to primary standards when applicable: synthetic Al_2O_3; fayalite; hematite, Elba; synthetic MgO; synthetic $SrSO_4$; synthetic TiO; and synthetic ZrO_2. ZAF corrections, according to the procedure of Pouchou & Pichoir (1991), were applied to account for matrix effects.

Mineral formula recalculations

Biotite – *apfu* were calculated on the basis of 12 anions per formula unit. H calculated by stoichiometry. Lithium estimated by equation $0.289SiO_2$–9.658 (Tischendorf *et al*. 1997).

Tourmaline – *apfu* were calculated on the basis of 31 total anions. Li_2O, H_2O, and B_2O_3 were calculated by stoichiometry. Water was measured by loss on ignition (LOI). Water determined by LOI was close to H_2O calc. We infer that there is only a small amount of O_2 at the V-site and therefore none of the tourmaline is oxy-schorl.

Feldspar – *apfu* were calculated based on eight oxygen atoms per formula unit; beryl – *apfu* based on 18 anions and Be calculated by stoichiometry; fluorite – *apfu* based on two F; and ilmenite–pyrophanite – *apfu* based on three anions.

Direct-coupled plasma spectrometry

Direct-coupled Plasma Spectrometry (DCP) analyses for Li in tourmaline were performed with a Beckman Spectraspan V DCP. The detection limit for Li is 2 ppb.

Whole rock fusion ICP analyses

Whole rock analyses were performed at the ACTLABS analytical facility in Ontario, Canada. The analytical package uses fusion ICP-OES for the major elements and ICP-MS for trace elements. Detection limits for the elements analyzed ranged from 0.001 to 30 ppm.

Titration for Fe^{2+} Fe^{3+}

Iron oxide titrations were performed on samples according to Wilson's method (1955), which utilizes oxidation of Fe^{2+} by ammonium metavanadate and back titrating the excess with ferrous ammonium sulfate.

Water determined by loss on ignition

The water content of 10 selected tourmaline crystals from miarolitic cavities was measured by loss on ignition (LOI) using powdered samples, which were heated under protective atmosphere to 900 °C for 12 hours.